NASA/TP—2019–220130

Real-Time Modeling of Thermal Interactions in Cryogenic Ball Bearings

P.K. Gupta
PKG Inc., Clifton Park, New York

H.G. Gibson
Marshall Space Flight Center, Huntsville, Alabama

March 2019

The NASA STI Program…in Profile

Since its founding, NASA has been dedicated to the advancement of aeronautics and space science. The NASA Scientific and Technical Information (STI) Program Office plays a key part in helping NASA maintain this important role.

The NASA STI Program Office is operated by Langley Research Center, the lead center for NASA's scientific and technical information. The NASA STI Program Office provides access to the NASA STI Database, the largest collection of aeronautical and space science STI in the world. The Program Office is also NASA's institutional mechanism for disseminating the results of its research and development activities. These results are published by NASA in the NASA STI Report Series, which includes the following report types:

- TECHNICAL PUBLICATION. Reports of completed research or a major significant phase of research that present the results of NASA programs and include extensive data or theoretical analysis. Includes compilations of significant scientific and technical data and information deemed to be of continuing reference value. NASA's counterpart of peer-reviewed formal professional papers but has less stringent limitations on manuscript length and extent of graphic presentations.

- TECHNICAL MEMORANDUM. Scientific and technical findings that are preliminary or of specialized interest, e.g., quick release reports, working papers, and bibliographies that contain minimal annotation. Does not contain extensive analysis.

- CONTRACTOR REPORT. Scientific and technical findings by NASA-sponsored contractors and grantees.

- CONFERENCE PUBLICATION. Collected papers from scientific and technical conferences, symposia, seminars, or other meetings sponsored or cosponsored by NASA.

- SPECIAL PUBLICATION. Scientific, technical, or historical information from NASA programs, projects, and mission, often concerned with subjects having substantial public interest.

- TECHNICAL TRANSLATION. English-language translations of foreign scientific and technical material pertinent to NASA's mission.

Specialized services that complement the STI Program Office's diverse offerings include creating custom thesauri, building customized databases, organizing and publishing research results…even providing videos.

For more information about the NASA STI Program Office, see the following:

- Access the NASA STI program home page at <http://www.sti.nasa.gov>

- E-mail your question via the Internet to <help@sti.nasa.gov>

- Phone the NASA STI Help Desk at 757–864–9658

- Write to:
  NASA STI Information Desk
  Mail Stop 148
  NASA Langley Research Center
  Hampton, VA 23681–2199, USA

NASA/TP—2019–220130

Real-Time Modeling of Thermal Interactions in Cryogenic Ball Bearings

P.K. Gupta
PKG Inc., Clifton Park, New York

H.G. Gibson
Marshall Space Flight Center, Huntsville, Alabama

National Aeronautics and
Space Administration

Marshall Space Flight Center • Huntsville, Alabama 35812

March 2019

Available from:

NASA STI Information Desk
Mail Stop 148
NASA Langley Research Center
Hampton, VA 23681–2199, USA
757–864–9658

TABLE OF CONTENTS

LIST OF FIGURES

LIST OF FIGURES (Continued)

LIST OF TABLES

LIST OF ACRONYMS

ADORE	Advanced Dynamics of Rolling Elements
BSMT	bearing and seal material tester
LOX	liquid oxygen
MSFC	Marshall Space Flight Center
REFPROP	Reference Fluid Thermodynamic and Transport Properties Database
SHABERTH	Shaft Bearing Thermal (model)
SINDA	Systems Improved Numerical Differencing Analyzer

NOMENCLATURE

A	area (m^2)
C_D	drag coefficient
c	clearance (m) between the rotating cylindrical surface and stationary housing
c_p	specific heat (J/kg/K)
D	diameter (m)
dT/dx	temperature gradient
F	friction force (N)
F'	friction force per unit area (N/m^2)
f	friction factor
h	heat transfer coefficient (W/m^2/K)
k	thermal conductivity (W/m/K)
M	moment (N.m)
m	mass fluid flow rate (kg/s)
Nu	Nusselt number
Pr	Prandtl number
q	heat flux (W)
q_{CR}	heat generation at the cage to race interface
q_{ReR}	total heat generation in the rolling element to race contact
Re	Reynolds number
r	radius (m)

NOMENCLATURE (Continued)

T	temperature (K)
Ta	Taylors number
T_o	surface temperature
T_∞	fluid temperature
t	time (s)
U	mass average velocity of fluid
u	sliding velocity (m/s)
V	velocity (m/s)
Wd	tire axis
y	axis of the toroid
Ω	race speed (rpm)
μ	viscosity (Pa.s)
ρ	density (kg/m^3)
ω	angular velocity (rad/s)

TECHNICAL PUBLICATION

REAL-TIME MODELING OF THERMAL INTERACTIONS IN CRYOGENIC BALL BEARINGS

1. INTRODUCTION

Rolling element bearings on the main shaft of low- and high-pressure turbopumps, which supply the cryogenic propellants to the Space Shuttle main engine, are critical elements of the entire propulsion system. Failure of these bearings generally leads to catastrophic results. Since the cryogenic fluid flows through the bearings, no external lubricant to enhance the tribological characteristics at the rolling element to race interface may be supplied to the bearing. It is essential that the bearings survive the relatively high traction at the rolling element to race interface during the duty cycle. While thermal interactions in oil-lubricated rolling bearings in gas turbine engines are important to ensure acceptable material and lubricant behavior, realistic modeling of contact heat generation at the rolling element to race contacts is significant in maintaining the liquid state of the cryogenic fluid flowing through the turbopump bearings in the Space Shuttle main engine. Thus, realistic modeling of thermal interactions in cryogenic bearings has substantial practical significance.

As discussed in a historical perspective presented by Gibson et al.,[1] most of the pioneering development work related to rolling bearings for cryogenic applications was carried out at NASA Marshall Space Flight Center (MSFC) during the 1980s and 1990s. The starting point was the development of a unique test rig to experimentally evaluate the performance of ball bearings in a cryogenic environment. The objective was to experimentally measure the performance parameters to further develop the available computer codes for bearing performance modeling, such as the Shaft Bearing Thermal (SHABERTH) model,[2] Systems Improved Numerical Differencing Analyzer (SINDA),[3] and Advanced Dynamics of Rolling Elements (ADORE).[4] At the time, with significant limitations of the modeling tools and the available computing hardware, and with due recognition to the extremely critical nature of the application, a significant emphasis was on experimental evaluation of bearing geometries and materials. Perhaps, the most significant outcome of the initial bearing test results was the successful demonstration of the benefits of using silicon nitride balls in terms of reduced wear and contact heat generation.[5] Subsequent testing of hybrid bearings has further proven the improved performance of hybrid bearings in a cryogenic environment.[6]

In terms of dynamic performance modeling, particularly when the bearing is subjected to rapid accelerations, the traction slip behavior in the ball/race contact is a significant input.[4] The traction slip relationship controls both the steady-state slip and frictional heat generation at the ball/race contacts. Also, the possibility of ball skid and resulting wear is related to the traction slip relationship. Based on a traction tester developed by Tevaarwerk,[7] Chang et al.[8] have examined such a behavior in rolling-sliding contacts operating in a liquid oxygen (LOX) environment. In addition to examining surface damage and investigating scuffing as a function of surface roughness, this work has also published traction data as a function of a slide-to-roll ratio at different rolling velocities. The output from this investigation serves as a significant input to the current bearing modeling tools.

While the NASA test rig, commonly referred to as BSMT (bearing and seal material tester) for testing ball bearings in a cryogenic environment, is described by Gibson,[5] Moore[9] has extensively documented the experimental data generated over a decade at the NASA laboratories. In addition, this work includes a thorough review of the modeling capabilities available at the time. While modeling of cage forces and the resulting dynamic interactions were modeled with ADORE,[4] the thermal solutions based on quasi-static bearing analysis, as provided by SHABERTH,[2] were interfaced with SINDA[3] to model the steady-state thermal behavior of a ball bearing in a cryogenic environment. Subsequent to this work, Gibson et al.[10] have also presented the bearing testing work done at MSFC, emphasizing the fact that the bearings support combined thrust and radial loads, and operate at high speed with high wear resistance under no lubrication.

True real-time dynamic analysis of bearing motion, as measured by the NASA test rig, requires a real-time integration of the classical differential equations of motion of bearing motion, as formulated in ADORE,[4] over extensive time domain. Unfortunately, due to limitations in numerical processing and available computing hardware, such a performance simulation could not be obtained at the time. Evaluation of bearing performance was therefore solely based on experimental investigations. Recent advances in both vector processing and several orders of magnitude increase in computing speed have made the compute intensive dynamic performance modeling of rolling bearings, as structured in ADORE,[4] possible within a reasonable amount of computing effort. In addition, the advances in computing technology have made the coupling of the transient mechanical and thermal interactions possible to provide a true real-time performance simulation of a rolling bearing under time-varying mechanical and thermal operating environments. The objective of the current investigation is, therefore, to demonstrate such modeling capabilities and provide experimental validation of model predictions with real-time ball bearing performance data measured with the NASA BSMT rig. It is expected that, in addition to cryogenic bearings, such a validation shall demonstrate the practical significance of current advances in modeling the dynamic behavior for any rolling bearing application in a complex operating environment.

2. EXPERIMENTAL

Experimental bearing performance data for validation of model predictions was collected at MSFC. Overview of BSMT, the test bearings, and experimental procedures are outlined below.

2.1 Bearing and Seals Material Tester

A schematic of the BSMT is shown in figure 1. The tester houses four test bearings and uses LOX as a coolant following through the bearings operating at 30,000 rpm for a predetermined amount of time. In addition to precise measurements of pressure and temperature, the tester has a subcooling capability to ensure that after a rise in temperature, due to heat generation in the bearing, LOX stays in a liquid state. Although for brevity, only the temperature sensors are shown in figure 1. LOX pressures are also monitored at various points in the tester. The LOX properties in the range of experimental conditions, as documented in section 2.5, are used to estimate the amount of heat generated in the bearing transferred to the circulating LOX.

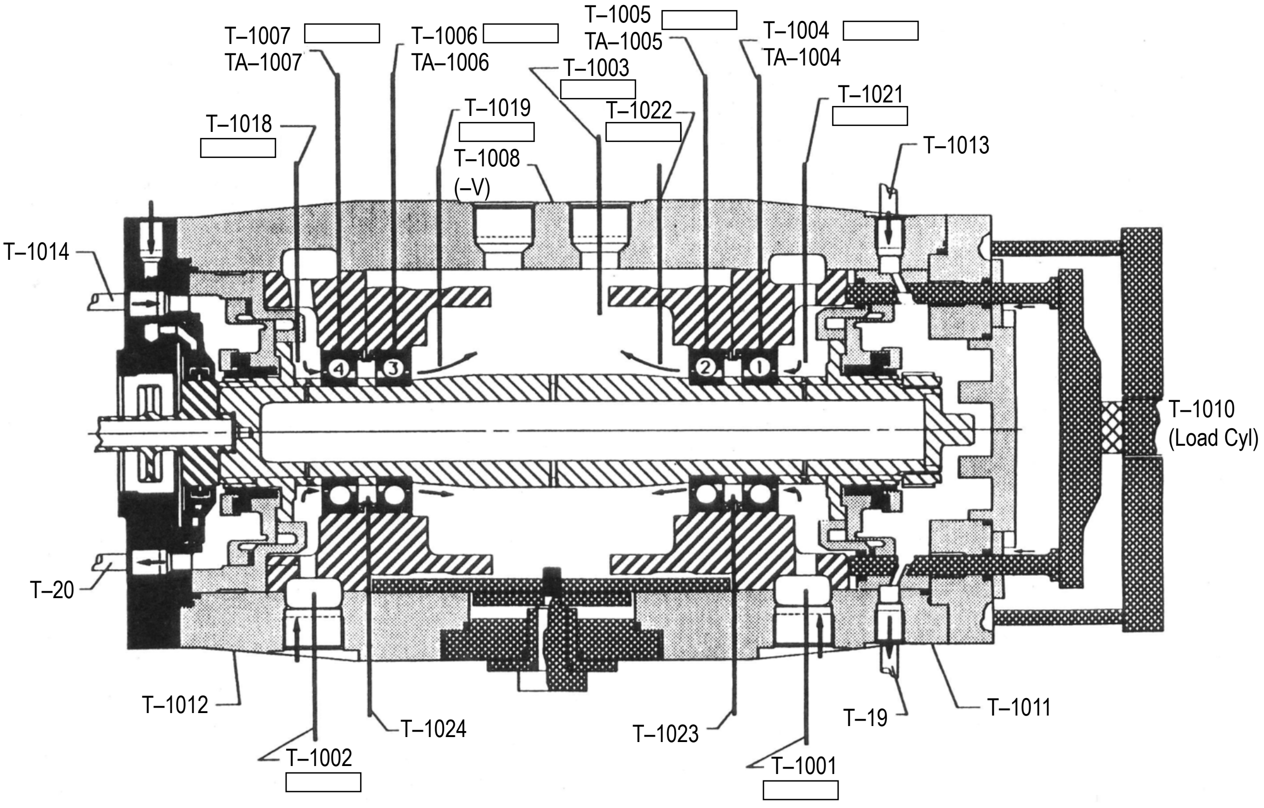

Figure 1. Schematic of NASA BSMT.

2.2 Test Bearings

Bearing performance is measured for two sets of four bearings. The first set consists of all-steel bearings while the second set consists of hybrid bearings with silicon nitride balls. A geometrical overview of the test bearings is documented in table 1.

Table 1. Test bearing materials and geometries.

Parameter	Bearing Set No. 1	Bearing Set 2 No. 2
Ball material	440C	Silicon nitride
Race material	440C	CRB–7
Cage material	Armalon	Armalon
Number of balls	13	13
Bore (mm)	57.2567	57.2567
Ball Diameter (mm)	12.70	12.70
Outer race curvature factor	0.550	0.530
Inner race curvature factor	0.530	0.530

2.3 Ball/Race Traction

Traction in the concentrated ball/race contact is perhaps the most significant parameter that controls the dynamic interactions in a ball bearing. In the current investigation, LOX simply flows through the bearing and there is no external lubricant at the ball to race contact. Tevaarwerk[7] developed a traction tester consisting of a concentrated rolling/sliding contact formed by a toroidal specimen pressed against a tire-shaped specimen mounted on a high-speed spindle. The contact load is applied in terms of simple dead weights and the contact is flooded with LOX. A schematic of the tester is presented in figure 2. The toroid is driven by the traction generated at the toroid to tire conjunction. When the axis of the toroid, y, is parallel to the tire axis, Wd, the conjunction is almost in pure rolling. Rotation of the toroid about the z axis introduces skew of the toroid axis from the tire axis, which results in sliding at the conjunction. The resulting traction force is picked up by a piezoelectric load sensor. LOX is supplied from the top of the toroid to cool and lubricate the toroid/tire conjunction and also the toroid bearings. The radius of the cylindrical tire is 50 mm while that of the toroid is 10 mm. Using this tester, Chang et al.[8] investigated frictional interactions between steel versus steel and silicon nitride versus steel contacts in a LOX environment. A series of tests were done with varying levels of surface finishes at different rolling velocities, while the applied load was set at 400 N. This resulted in a contact stress of 2.2 GPa for the AISI 440C samples, and 2.9 GPa for the steel tire against silicon nitride toroid. Traction was measured as a function of a slide-to-roll ratio and the onset of scuffing was investigated. In the current modeling effort, the data of interest is traction behavior, with relatively smooth surfaces at high rolling velocity. Figure 3 shows a typical data set for a 440C versus 440C rolling/sliding contact. At very low slide-to-roll ratios, the traction coefficient increases almost linearly until it reaches a maximum value of about 0.05 at a slide-to-roll ratio of about 0.0015, and then it stays relatively constant with an increasing slide-to-roll ratio until the onset of scuffing at slide-to-roll ratios of 0.01.

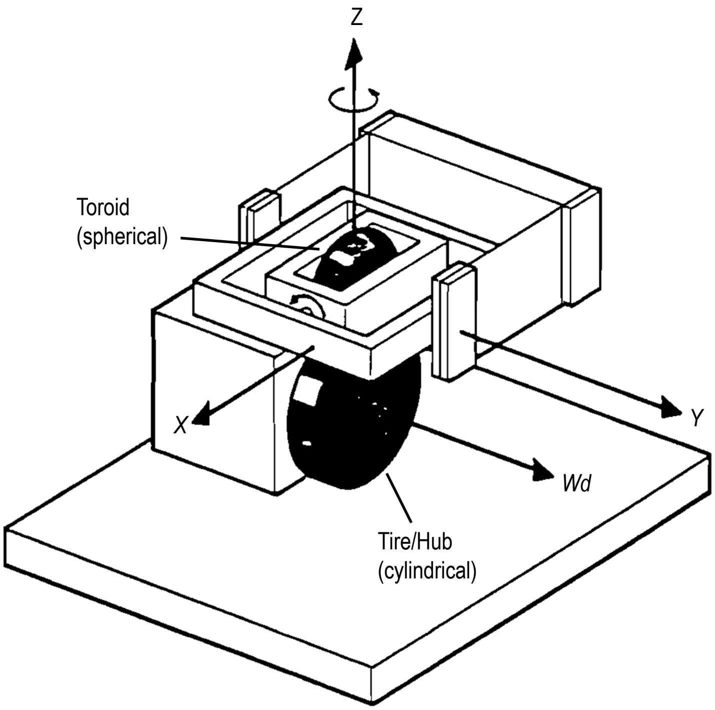

Figure 2. Schematic of traction tester developed by Tevaarwerk.[7]

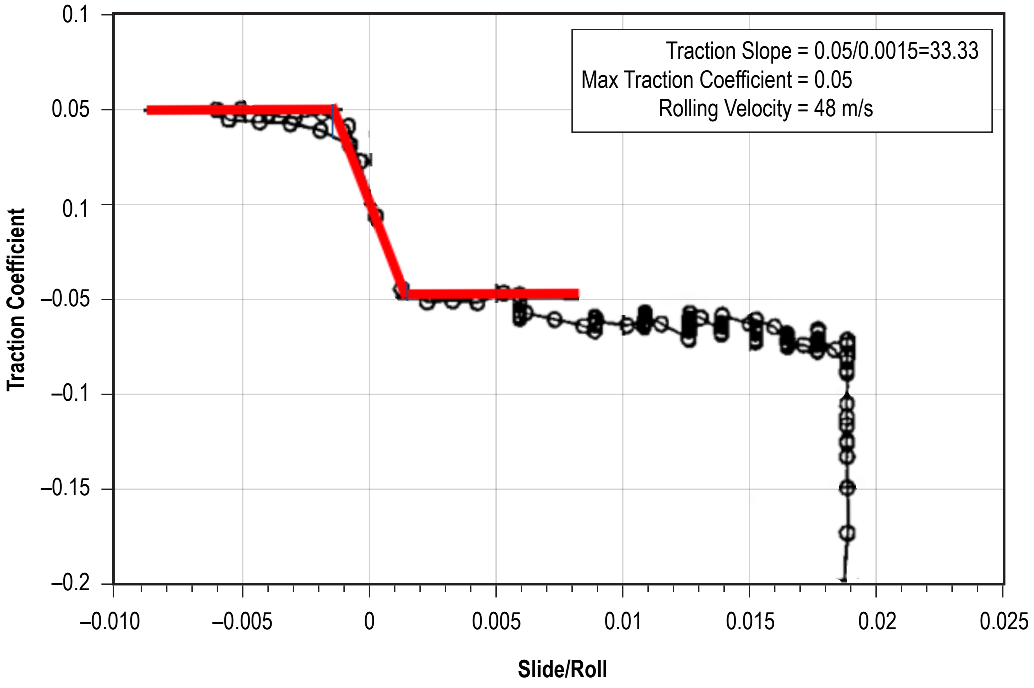

Figure 3. 440C versus 440C traction slip behavior at a contact stress of 2.2 GPa.

A second series of tests were conducted for a silicon nitride toroidal specimen against a 440C steel tire-shaped specimen. As shown in figure 4, the traction coefficient again increases almost linearly with an increasing slide-to-roll ratio, but the maximum traction coefficient is only 0.025, which is reached again at a slide-to-roll ratio of 0.0015 and the onset of scuffing moved further out to a higher slide-to-roll ratio. This reduction in traction is significant in modeling the dynamic behavior of a hybrid bearing in a LOX environment.

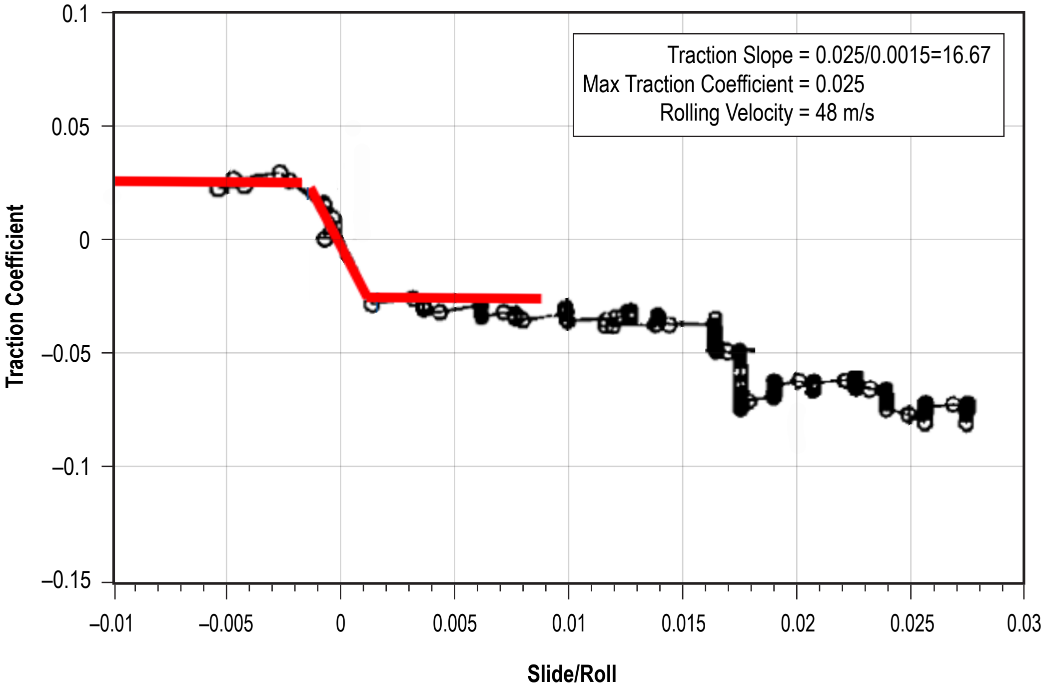

Figure 4. Traction-slip behavior of a silicon nitride versus 440C steel contact in LOX environment at a contact stress of 2.9 GPa.

2.4 Cage Friction

The contacts at the ball/cage and cage/race interfaces are very lightly loaded but they are highly dynamic in nature. Unlike the ball/race contacts, these contacts are simple high-speed sliding contacts. Therefore, the frictional interactions may be modeled by a simple friction coefficient. In the absence of any available data on the friction coefficient for the armalon/440C and armalon/silicon nitride contacts, a constant friction coefficient of 0.05 is assumed in both 440C and hybrid bearings.

2.5 Liquid Oxygen Properties

Perhaps, the most up-to-date properties of LOX are compiled in the software, REFPROP (Reference Fluid Thermodynamic and Transport Properties Database, version 10), distributed by the National Institute of Standards and Technology.[11] The LOX pressure and temperature were regulated so that LOX stays in liquid form under all test conditions per the LOX boiling point and pressure relationship shown in figure 5. For the simulation of churning and drag losses, the required properties are density and viscosity at applicable pressure and temperature, which are shown in figures 6 and 7, respectively.

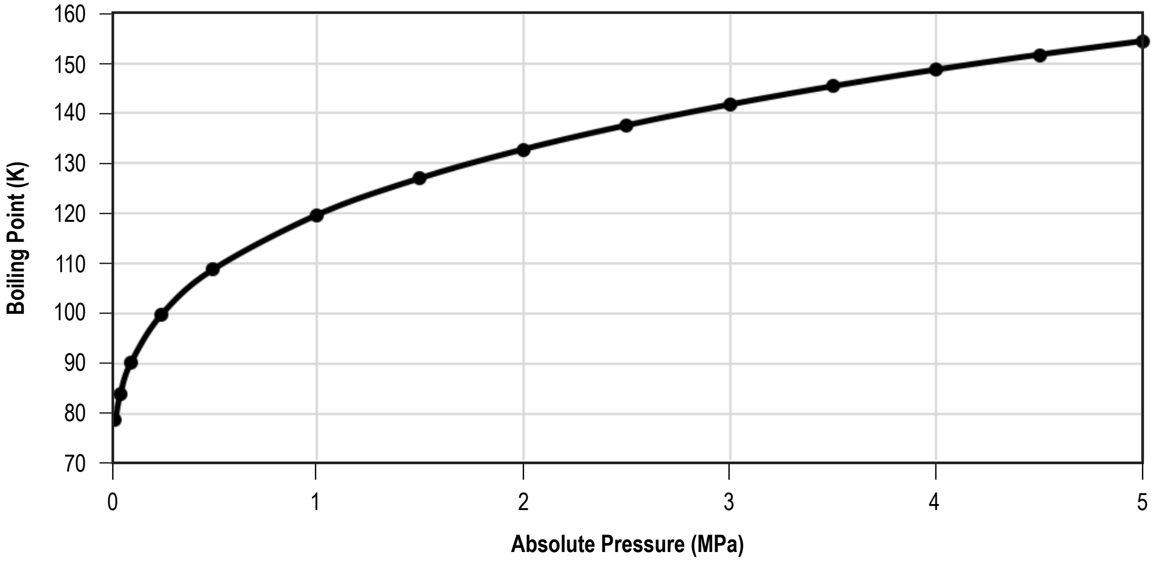

Figure 5. LOX boiling point as a function of pressure.

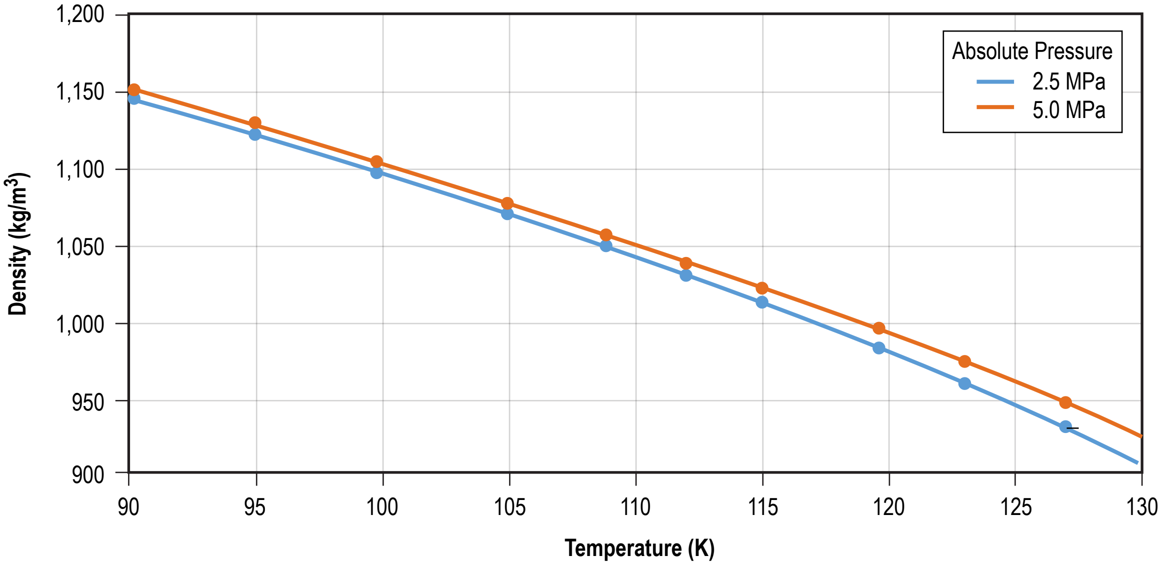

Figure 6. Variation in LOX density as a function of pressure and temperature.

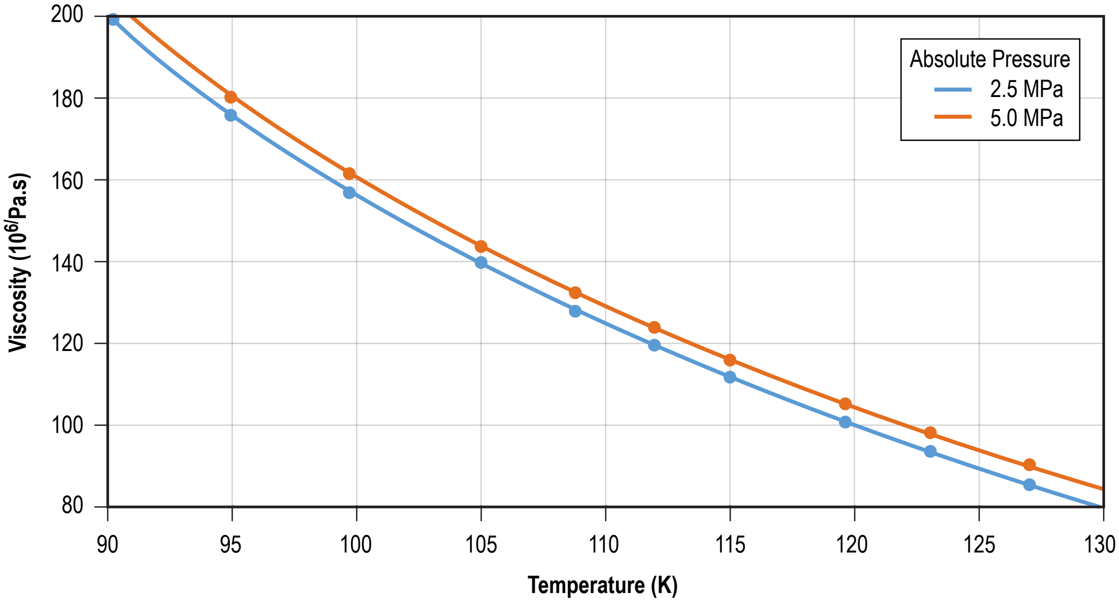

Figure 7. Variation in LOX viscosity with temperature and pressure.

For the purpose of modeling thermal interactions which provide applicable temperature fields corresponding to the computed heat generation, the required properties are specific heat and thermal conductivity. Again, these properties also exhibit a variation as a function of pressure and temperature. These variations are shown in figures 8 and 9, respectively, for the specific heat and thermal conductivity.

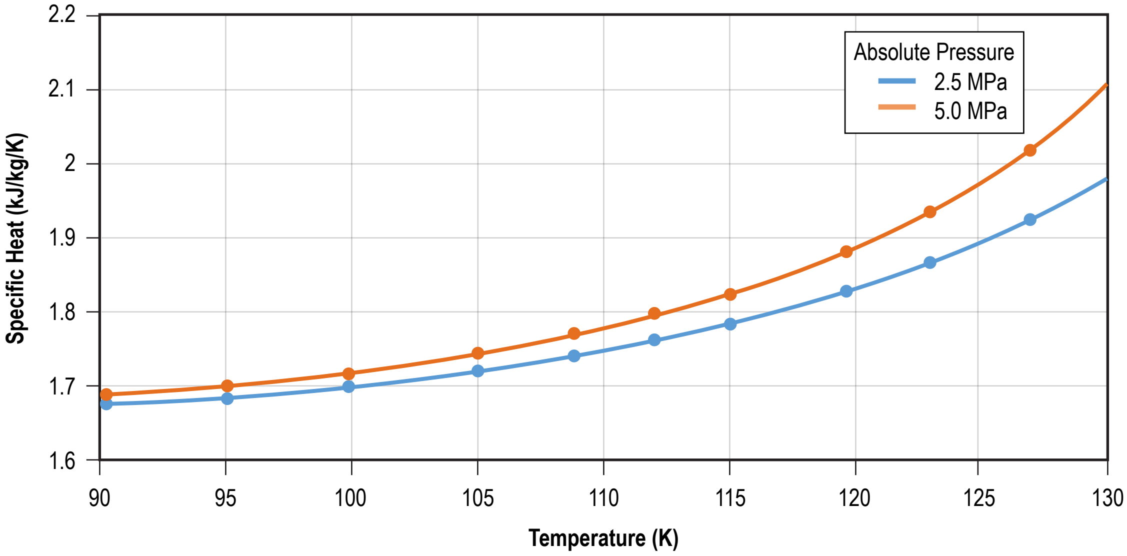

Figure 8. Variation in LOX specific heat as a function of pressure and temperature.

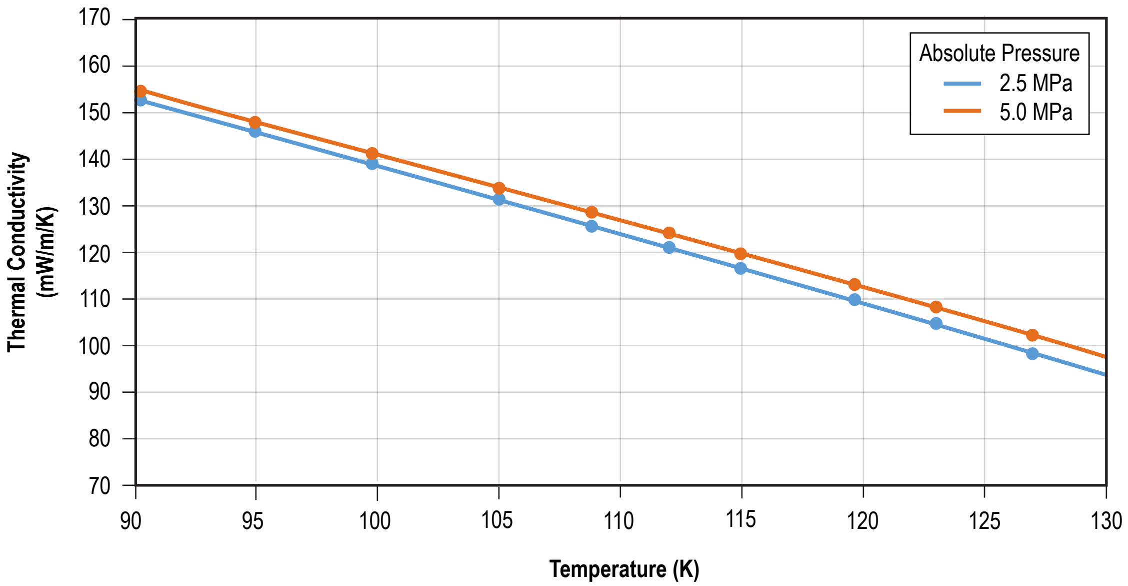

Figure 9. LOX thermal conductivity as a function of pressure and temperature.

2.6 Test Procedure

Unlike the common bearing tests, which often run at a constant speed for several hours or sometimes several days, the test sequence for a typical test in the current investigation lasts for about 3 to 4 minutes. The sequence starts when an acceleration is applied on the inner race to bring the bearing to the operating speed of about 30,000 rpm in about 1 minute. The bearing then runs for about 2 to 3 minutes as the operating parameters, primarily the operating temperatures at the various points in the test rig, stabilize to a steady value. Figure 10 shows a typical test sequence where the recorded variation in temperatures, as obtained for a few of the temperature sensors, is plotted as a function of time.

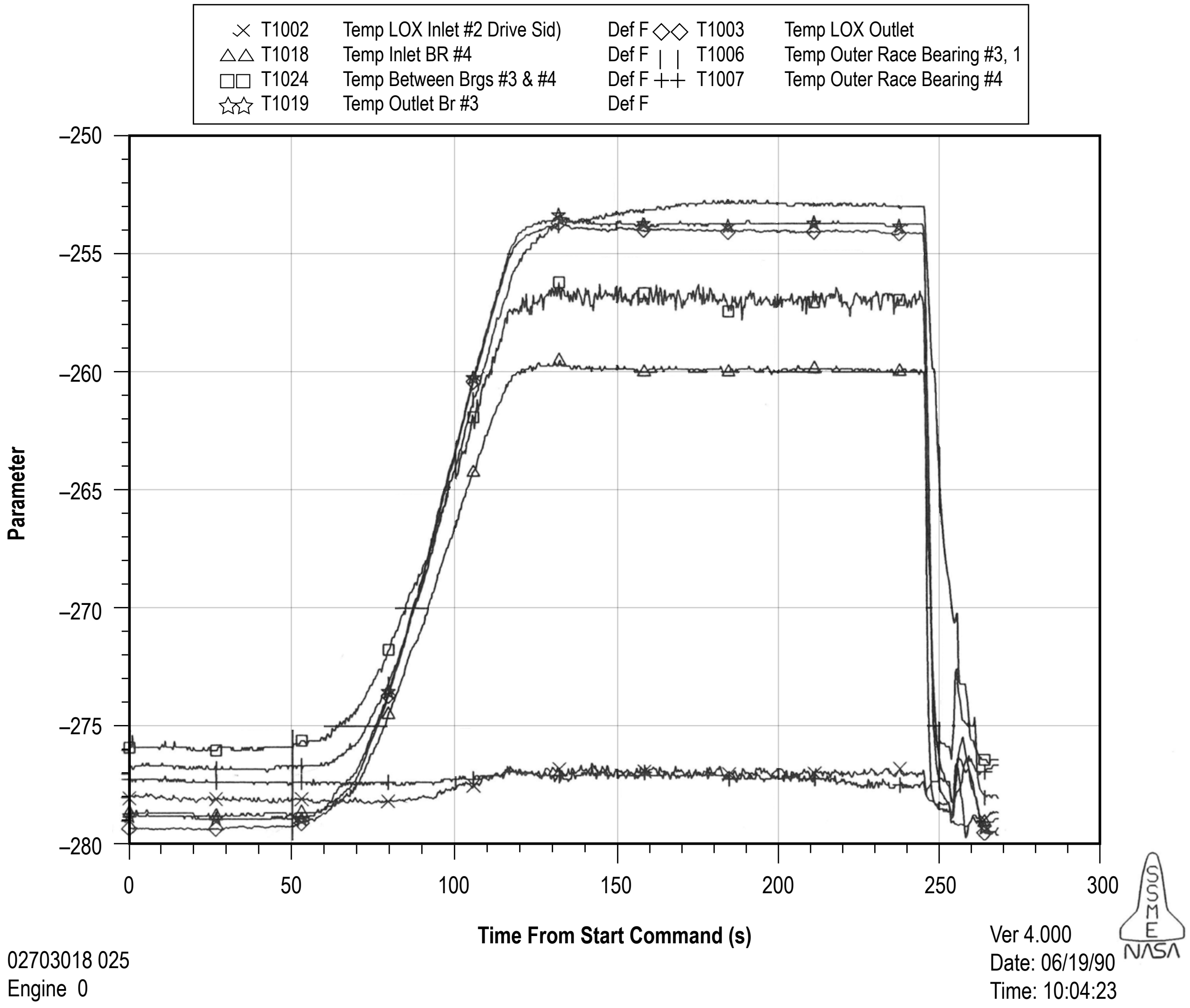

Figure 10. A typical test sequence showing variation in temperature (ºF) as a function of time.

While a large number of tests were carried out for both all-steel and hybrid bearings, the number of tests selected for validation in the present investigation are tabulated in tables 2 and 3, respectively, for the all-steel and hybrid bearings.

Table 2. Experimental data for 440C bearings.

Test Identification	**310301**	**310402**	**310501**	**310703**	**310802**	**310901**
Speed, Krpm	25	30	30	30	30	30
Thrust load, kN (lbf)	5.338 (1,200)	6.672 (1,500)	6.672 (1,500)	6.672 (1,500)	6.672 (1,500)	6.672 (1,500)
LOX flow rate, L/s (lbm/s)	1.827 (4.6)	1.827 (4.6)	1.827 (4.6)	1.827 (4.6)	1.827 (4.6)	1.827 (4.6)
Brg 1 LOX inlet temp, K (ºF)	118.15 (–247)	122.04 (–240)	120.37 (–243)	112.59 (–257)	119.82 (–244)	118.15 (–247)
Brg 1 LOX exit temp, K (ºF)	120.17 (–243)	124.82 (–235)	123.15 (–238)	120.93 (–242)	122.04 (–240)	120.37 (–243)
Brg 2 LOX exit temp, K (ºF)	122.04 (–240)	129.26 (–227)	128.15 (–229)	127.04 (–231)	126.48 (–232)	124.82 (–235)
Brg 4 LOX inlet temp, K (ºF)	118.15 (–247)	122.59 (–239)	120.93 (–242)	119.26 (–245)	119.26) (–245)	116.48 (–250)
Brg 4 LOX exit temp, K (ºF)	118.71 (–246)	123.71 (–237)	123.71 (–237)	120.37 (–243)	120.93 (–242)	118.71 (–246)
Brg 3 LOX exit temp, K (ºF)	123.15 (–238)	129.82 (–226)	128.15 (–229)	125.93 (–233)	127.04 (–231)	124.82 (–235)
Brg 1 and 4, LOX inlet pressure, MPa (lbf/in^2)	4.240 (615)	3.861 (560)	4.275 (620)	4.275 (620)	3.585 (520)	2.930 (425)
Brg 2 and 3, LOX exit pressure, MPa (lbf/in^2)	3.964 (575)	3.585 (520)	3.930 (570)	3.930 (570)	2.896 (420)	2.482 (360)

Table 3. Experimental data for hybrid bearings (440C races, silicon nitride balls).

Test Identification	**270301**	**270401**	**270501**	**270601**	**270705**	**270802**
Speed, Krpm	25	26	28.25	30.30	30.20	29.90
Thrust load, kN (lbf)	6.672 (1,500)	8.007 (1,800)	8.007 (1,800)	8.007 (1,800)	8.007 (1,800)	8.007 (1,800)
LOX flow rate, L/s (lbm/s)	2.661 (6.7)	2.582 (6.5)	2.582 (6.5)	2.582 (6.5)	2.582 (6.5)	2.582 (6.4)
Brg 1 LOX inlet temp, K (ºF)	110.87 (–260)	118.15 (–247)	119.26 (–245)	119.94 (–244)	120.71 (–242)	123.71 (–237)
Brg 1 LOX exit temp, K (ºF)	111.54 (–259)	118.93 (–246)	122.04 (–240)	123.68 (–237)	123.63 (–237)	126.48 (–232)
Brg 2 LOX exit temp, K (ºF)	114.48 (–254)	121.87 (–240)	123.98 (–236)	125.64 (–233)	126.16 (–232)	129.26 (–227)
Brg 4 LOX inlet temp, K (ºF)	110.98 (–260)	117.21 (–249)	118.21 (–247)	119.02 (–245)	119.43 (–245)	122.59 (–239)
Brg 4 LOX exit temp, K (ºF)	112.65 (–257)	120.26 (–243)	121.43 (–241)	122.74 (–239)	122.71 (–239)	125.93 (–233)
Brg 3 LOX exit temp, K (ºF)	114.37 (–254)	121.48 (–241)	123.71 (–237)	125.76 (–233)	125.88 (–233)	128.71 (–228)
Brg 1 and 4, LOX inlet pressure, MPa (lbf/in^2)	3.103 (450)	3.061 (444)	3.054 (443)	3.068 (445)	3.068 (445)	3.068 (445)
Brg 2 and 3, LOX exit pressure, MPa (lbf/in^2)	2.896 (420)	2.827 (410)	2.827 (410)	2.827 (410)	2.827 (410)	2.827 (410)

3. MODELING OF BEARING PERFORMANCE

As discussed earlier, bearing performance modeling in the present investigation is based on the bearing dynamics model ADORE.[4] The dynamic operating conditions, such as race acceleration to operating speed, are input into the dynamic equations of motion, which are integrated in real-time to obtain the bearing performance simulation as measured in the tester. In addition to solving the mechanical interactions for computation of applied forces and moments, a time-averaging algorithm is developed to couple the transient thermal interactions to obtain an integrated mechanical and thermal solution to steady-state bearing heat generation. The predicted heat generation is then validated against the experimental data to establish practical significance of the model. The various steps in the modeling process are discussed below.

3.1 Modeling of Input Race Acceleration

The transient part of the test sequence in figure 10 is modeled by imposing a constant angular acceleration on the inner race as the race speed increases from Ω_1 at time t_1 to Ω_2 at time t_2 as shown in figure 11:

$$\dot{\Omega} = \frac{\Omega_2 - \Omega_1}{t_2 - t_1} \qquad t_1 \le t \le \mathrm{t}_2 \tag{1a}$$

$$\dot{\Omega} = 0 \qquad t < t_1 \text{ and } t > t_2 . \tag{1b}$$

In the current application, $t_1 = 0$, $t_2 = 60$ s, $\Omega_1 = 0$, and Ω_2 = operating speed.

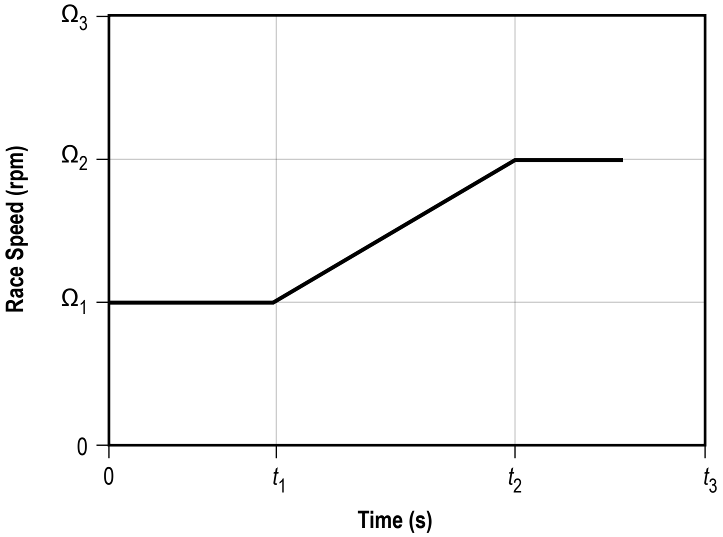

Figure 11. Schematic of the model for inner race speed variation.

3.2 Elements of Heat Generation in Rolling Bearings

Thermal interactions in a rolling bearing very often control the overall performance of a rolling bearing. The heat generated between interacting bearing elements travels through the bearing to the support system, and in the process, alters the temperature field in the bearing. The changes in operating temperatures affect both the internal geometry and material properties, which alter interaction between bearing elements to modify the bearing load distribution, which in turn, feeds back to heat generation. Such an iterative process continues until all solutions converge to steady-state conditions. In the event convergence cannot be reached, the bearing experiences a thermal instability and failure is eminent. Thus, realistic thermal modeling is a key element in the development of bearing performance simulation models. For a cryogenic bearing in a turbopump, where the cryogenic fluid flows through the bearing, heat generation is particularly important to ensure that the fluid does not vaporize and obstruct the flow. In other words, a realistic estimate of heat generation provides guidance for the required subcooling of the fluid for satisfactory operation.

In a rolling bearing in a LOX environment, there are essentially two types of heat generation: frictional heat generated between all interacting bearing elements, and LOX churning and drag as the rolling elements and cage travel through the bearing. While the rolling elements maintain contact with the races, support all the applied load, and roll over the races at relatively high speed, the purpose of the cage is to prevent contact between the rolling elements and avoid the very high-speed sliding between the rolling elements. However, introduction of the cage introduces frictional interaction between the rolling element and cage, and also the cage and race, when the cage is guided on one of the races. Frictional heat is generated at each of these interactions. In addition, both the rolling elements and cage travel through the circulating LOX, which produces heat due to churning and drag.

3.2.1 Rolling Element to Race Contacts

Rolling element to race contacts support all the applied load and the high-speed rotational motion between the outer and inner races. As a result of elastic deformation, the contact area between ball and race is elliptical in shape in ball bearings. Lubrication of these contacts has been known to be the most critical factor in controlling bearing performance. In the current cryogenic application, however, there is no lubricant. Compared to conventional lubricants, the hydrodynamic film generated by LOX is quite small and therefore the contact is essentially metal to metal. The traction coefficient data discussed earlier in figures 3 and 4 perhaps provide the most realistic modeling of the frictional interactions.

By integrating the equations of motion in ADORE, the geometric interaction between the balls and races is known at any instant of time. This provides the applicable contact load and pressure at each contact. Likewise, the relative slip between the ball and races can be computed from the respective velocities. Since both the local pressure and sliding velocity vary from point-to-point in the contact area, the traction coefficient, and therefore the traction force, is computed at each point in contact per the traction slip relation presented in figures 3 and 4. The corresponding heat generation is then a product of the traction force and sliding velocity. An integration of this product over the contact area provides the total heat generation in the contact:

$$q_{ReR} = \int_A F'u \, dA \ , \tag{2}$$

where q_{ReR} is total heat generation in the rolling element to race contact, F' is the traction force per unit area at any incremental area in the contact, u is the sliding velocity, and A is the contact area.

This computation is performed at both inner and outer races for each rolling element. All the heat generations are then summed to compute total heat generation in the rolling element to race contacts.

3.2.2 Rolling Element to Cage Contacts

As the ball accelerates towards the cage pocket and ultimately collides in the cage pocket, a contact force is produced. The rotational motion of the ball produces slip, which leads to friction at the interface. Since these forces are highly dynamic in nature and quite small in magnitude in comparison to the load support forces at the rolling element to race contacts, ADORE models the contact as a simple point contact and the contact load is computed by the elastic solutions. In absence of any sliding friction data between the current materials, a constant friction coefficient of 0.05, is assumed for these contacts, as discussed earlier. The resulting friction force is simply the product of computed normal force and friction coefficient. Finally, the heat generation in the contact is a simple product of friction force and sliding velocity:

$$q_{ReC} = Fu \ , \tag{3}$$

where q_{ReC} is the heat generation, F is the friction force, and u is the sliding velocity.

Again, heat generation at all the rolling element to cage contacts is summed to obtain the total heat generation in all cage contacts.

3.2.3 Cage to Race Contacts

When the cage is guided on the race, the nature of cage to race contact is similar to that between the rolling element and cage; the contact forces are low and the contact is subject to pure sliding. Therefore, the treatment is identical to that discussed above for ball to cage contacts. The normal force is computed from an elastic contact solution between two cylindrical bodies. Again, similar to the ball to cage interface, the friction coefficient at this interface is assumed to be 0.05. Contact heat generation is then expressed by the relation similar to equation (3):

$$q_{CR} = Fu \ , \tag{4}$$

where q_{CR} is the heat generation, F is the friction force, and u is the sliding velocity at the cage to race interface.

Generally, the cage has two guiding lands, one on each side of the rolling elements. Heat generations on both lands are summed to estimate the total cage to race contact heat generation.

3.2.4 Churning and Drag Losses

When the LOX flows through the bearing, the bearing cavity is essentially filled with LOX and both the balls and cage have to travel through LOX. This generates drag forces and churning moments, which not only affect bearing element motion but significantly add to bearing heat generation. Realistic modeling of these interactions is essential in modeling both the bearing element motion and the overall heat generation. Primarily due to intricacies associated with internal geometry of a rolling bearing, precise modeling of the lubricant flow pattern is a very difficult task. A number of simplifying assumptions are necessary even in the most advanced computational fluid dynamics techniques. In view of these complications, modeling of drag forces and churning moments and the resulting power losses is a highly empirical art. In the present investigation, the available models based on classical laminar and turbulent flows[4] are used with an effective density and viscosity for the circulating fluid. Unlike the conventional bearings, since the entire bearing cavity is filled with LOX, the applicable fluid density and viscosity are simply determined from the LOX properties at applicable pressure and temperature as documented earlier. The key equations, as documented in the available literature,[4] are presented below for completeness.

Drag forces on balls are generally estimated by empirical drag coefficients for spherical bodies:

$$F_D = C_D \left[\frac{1}{2} \rho V^2 A \right] , \tag{5}$$

where F_D is the computed drag force, C_D is the drag coefficient, the experimentally measured values of which are documented by Schlichtig,[12] ρ is the effective density, V is the orbiting velocity, and A is the frontal area. The frontal area on the rolling element is the area subjected to drag; this is simply the rolling element face area minus the area covered by the cage. The drag coefficient is generally expressed as a function of Reynolds number, Re:

$$\mathrm{Re} = \frac{\rho V D}{\mu} . \tag{6}$$

Here, D is a characteristic length, which is the rolling element diameter, and μ is the fluid viscosity.

Based on a wide range of experimental data, Schlichtig[12] has plotted the drag coefficient as a function of Reynolds number for both spherical and cylindrical bodies. The data for spherical bodies, as applicable to ball bearings, are reproduced in figure 12. These data are interpolated to estimate applicable drag coefficient in the present investigation.

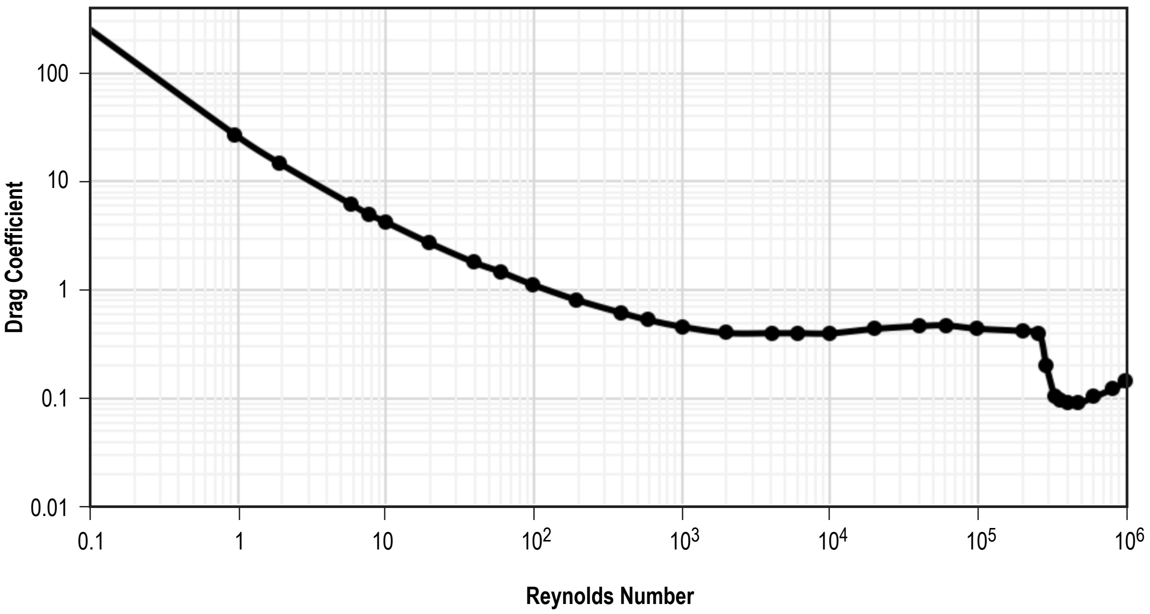

Figure 12. Drag coefficient as a function of Reynolds number for spherical bodies.[12]

The resulting power loss due to this drag is simply the drag force multiplied by the orbital velocity.

Churning moments are significant on the cage as it turns through the fluid. Normally, there will be a loss on both the cylindrical surface and end faces. An empirical formula for moment on the cylindrical surface is written as:

$$M_c = \frac{1}{2} f \rho U^2 A r \ , \tag{7}$$

where, ρ is the applicable density, U is the mass average velocity of fluid, A is the area, and r is a reference radius from center of rotation, and the friction factor, f, is defined as follows:

Vortex turbulent flow: $$\frac{f}{f_L} = 1.3\left(\frac{\text{Ta}}{41}\right)^{0.539474}\Bigg|_{\text{Ta}>41} \tag{8a}$$

Couette turbulent flow: $$\frac{f}{f_L} = 3\left(\frac{\text{Re}}{2{,}500}\right)^{0.85596}\Bigg|_{\text{Re}>2{,}500} \tag{8b}$$

Laminar friction factor: $$f_L = \frac{16}{\text{Re}}\Bigg|_{\text{Re}<2{,}500 \text{ or } Ta<41} \tag{8c}$$

Reynolds number: $$\mathrm{Re} = \frac{\rho r \omega c}{\mu} \tag{8d}$$

Taylors number: $$\mathrm{Ta} = \frac{\rho r \omega c}{\mu}\sqrt{\frac{c}{r}}\ . \tag{8e}$$

Generally, the reference radius, r, is the radius of the rotating cylindrical surface, and c is the effective clearance between the rotating cylindrical surface and stationary housing.

For typical high-speed rolling bearings, the flow on the cage surface is approximated as Coutte turbulent.

For the end surfaces of the cage, the churning moment is written as:

$$M_c = \frac{1}{2}\rho\omega^2 r^5 C_n \tag{9a}$$

$$C_n = 3.87 / \mathrm{Re}^{0.5} \text{ for laminar flow Re} < 300{,}000 \tag{9b}$$

$$C_n = 0.146 / \mathrm{Re}^{0.2} \text{ for turbulent flow Re} > 300{,}000 \tag{9c}$$

$$\mathrm{Re} = \frac{\rho r^2 \omega}{\mu} \text{ is the Reynolds number.} \tag{9d}$$

The effective radius, r, for the cage, which has the inner and outer radius, r_{in} and r_{out}, respectively, is approximated as:

$$r^5 = r_{\mathrm{out}}\left(r_{\mathrm{out}}^4 - r_{\mathrm{in}}^4\right) \text{ for laminar flow} \tag{10a}$$

$$r^5 = r_{\mathrm{out}}^{0.4}\left(r_{\mathrm{out}}^{4.6} - r_{\mathrm{in}}^{4.6}\right) \text{ for turbulent flow.} \tag{10b}$$

Although no explicit expressions for computing churning moment on the ball are available, the moment may be approximated by that occurring on a projected area normal to the ball angular velocity, which approximates it as a thin disk, with no cylindrical surface. Thus, equations (9a) to (9d) may be used.

The churning loss is simply the product of the computed churning moment and applicable angular velocity of rotation.

3.3 Time-Averaging of Heat Generations

Although churning and drag losses are unaffected by subtle speed variations due to mechanical interactions between bearing elements, the contact heat generations due to dynamic contact between rolling elements and cage, and also those between the cage and the guiding race, are highly dynamic in nature. Typical heat generations resulting from integration of the differential equations of motion appear as spikes over the base heat generation, as shown schematically in figure 13. While coupling of these dynamic interactions with thermal transients with a very large time scale results in a computationally inefficient stiff system, application of static thermal interactions results in unrealistic high-frequency temperature variations. Therefore, an approach based on step averaging of the heat generation produced by dynamic interactions is developed. As shown schematically in figure 13, for a selected step bounded by times t_{j-1} and t_j, the heat generation is averaged before applying a static thermal analysis:

$$\overline{q}_j = \frac{1}{\Delta t}\int_{t_{j-1}}^{t_j} q(t)\,dt \ , \tag{11}$$

where the thermal averaging step is defined as $\Delta t = t_j - t_{j-1}$.

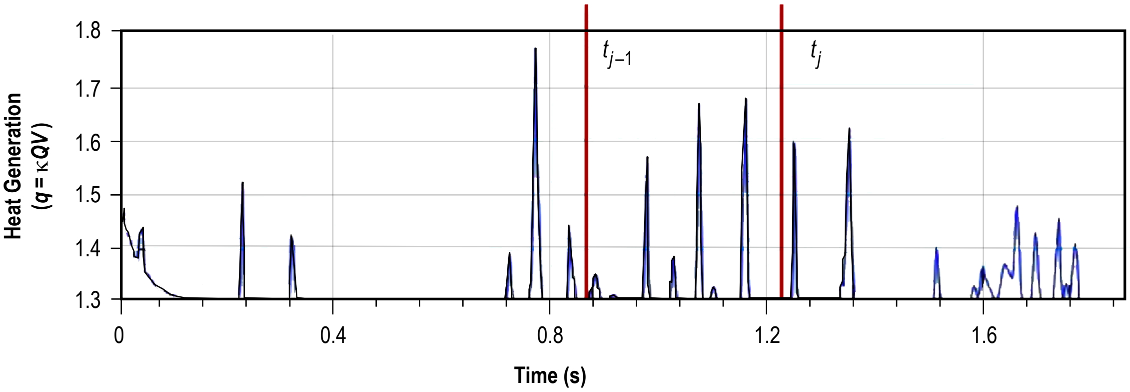

Figure 13. Schematic description of typical heat generation solution in a rolling bearing.

The averaging step is selected by trial and error. Generally, a time interval corresponding to about 10 revolutions of the bearing provides reasonable results.

Since the initial conditions for dynamic simulation of bearing performance are generally selected arbitrarily, the initial transients in the dynamic interactions may be insignificant. Therefore, these transients may be skipped before heat generation averaging is initiated for thermal analysis. Although under stable operation, the steady-state solutions do not depend on initial conditions, as will be demonstrated later.

3.4 Heat Transport and Modeling of Temperature Field

Once the heat generations at the various interfaces in the bearing are determined by the above step-averaging approach, a thermal analysis is required to compute the temperature field in the bearing. Due to obvious complexities associated with heat flow in the bearing, such an analysis is generally very complex; perhaps the best approach may be to carry out a finite element analysis. Coupling such an analysis with the time-varying solutions obtained by integrating the equations of motion of bearing elements further complicates the thermal analysis task. Thus, the simplified approach developed earlier by Gupta[13] is retained in the presented investigation. Aside from churning and drag effects, frictional heat is generated at the ball to race contacts. Depending on material properties of the balls and races, part of this heat is transferred to the bearing races, which in turn travels to the bearing support system, and the remainder goes to the balls, which is transferred to the circulating fluid. The simplified analysis developed by Gupta[13] is based on the following assumptions:

- Heat generated at rolling element to race contact travels via conduction to the rolling elements and races.

- All heat transferred to the races goes to the support system via conduction.

- Heat generated at all cage contacts is transferred via conduction to the cage and contacting elements.

- All heat transferred to the rolling elements and cage is transferred via convection to the circulating lubricant.

- The heat generated due to churning and drag is added to the heat in the circulating fluid and travels out of the bearing.

All conduction type heat transfer is based on the simple conduction equation:

$$q = -kA\frac{dT}{dx} \ , \tag{12}$$

where q is the heat flux, k is thermal conductivity, A is the effective area for heat flow, and dT/dx is the temperature gradient.

Convective heat transfer is modeled as

$$q = hA\left(T_o - T_\infty\right) \ , \tag{13}$$

where T_o is the surface temperature and T_∞ is the fluid temperature at exit. The heat transfer coefficient, h, is related by empirical equations in terms of the following dimensionless parameters:

$$\text{Reynolds number:} \quad \mathrm{Re} = \frac{\rho V D}{\mu} \tag{14a}$$

$$\text{Prandtl number:} \quad \mathrm{Pr} = \frac{\mu c_p}{k} \tag{14b}$$

$$\text{Nusselt number:} \quad \mathrm{Nu} = \frac{hD}{k} \ . \tag{14c}$$

The commonly used empirical correlations are documented in references 14 through 16. The correlation for spheres, as applicable to balls, is written as:

$$\mathrm{Nu} = \mathrm{Pr}^{0.3}\left(0.97 + \mathrm{Re}^{0.5}\right) \ . \tag{15}$$

The Reynolds number, as applicable to the balls, is based on ball orbital velocity. The cage in a ball bearing is essentially driven by the balls in the cage pockets. Although the cage is a cylindrical element, most of the convection is controlled by fluid flow through the pockets, which is quite complex. Therefore, in the present investigation, the Nusselt number for the cage is set equal to that computed for the balls. In addition, the race surface temperature is set equal to that computed for the ball surface. With these simplifying assumptions, the temperature field in the bearing relative to an input reference temperature is completely defined.

Finally, the total flux to circulating fluid in terms of the inlet and exit temperatures is

$$q = mc_p\left(T_{\text{exit}} - T_{\text{inlet}}\right) \ . \tag{16}$$

Since the heat transmitted to the races flows to the overall mounting system, computation of race temperature by simple radial conduction may be subject to substantial uncertainty. Therefore, an estimate of overall experimental bearing heat generation based on the measured temperature field is subject to significant uncertainty. However, since the fluid flow rate and input and exit temperatures are more precisely measurable, experimental estimate of the heat transferred to the circulating fluid, as defined above by equation (16), has the least uncertainty. It is, therefore, used to validate the model predictions.

3.5 Overall Model Implementation in ADORE

The above formulation of thermal interactions is implemented in the bearing dynamics code, ADORE,[4] which integrates the equation of motion of bearing elements to provide a real-time simulation of bearing performance. The implementation is schematically described in figure 14. From the prescribed operating conditions, bearing geometry, and material properties, which includes frictional behavior, the equations of motion are integrated to obtain the bearing motion, interacting loads, moments, and heat generation. The computed heat generation is time averaged, as discussed above, and then at the appropriate time, the thermal interaction analysis is carried out to calculate the temperature field in the bearing. The transient analysis is continued until the temperature fields stabilize to steady-state values. Under stable conditions, the solutions represent steady-state behavior of the bearing. When the temperature fields do not stabilize, a thermal instability is indicated.

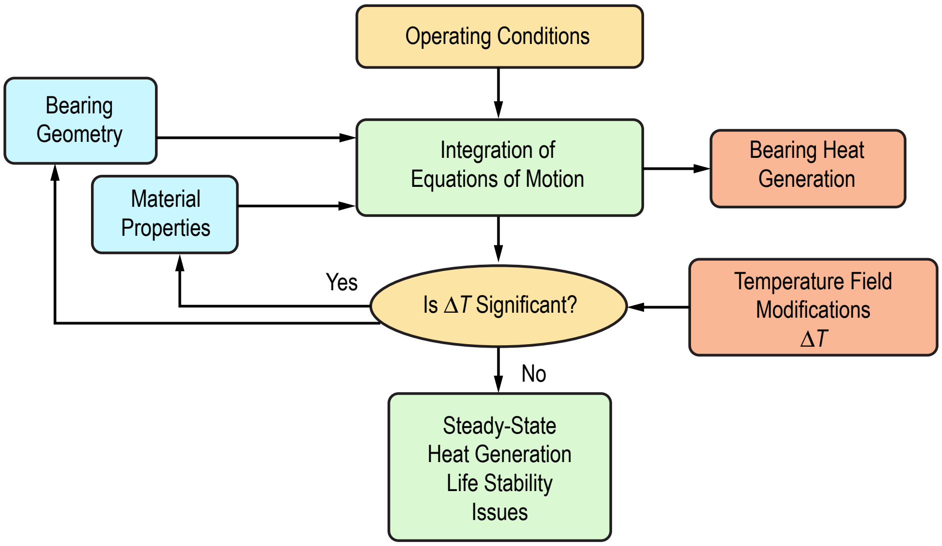

Figure 14. Schematic representation of thermal interaction analysis in ADORE.

4. RESULTS AND EXPERIMENTAL VALIDATION

For a typical test point, when the operating race speed is 30,000 rpm, the race speed variation as a function of time, as simulated in ADORE, with race acceleration described in figure 11, is shown in figure 15. From a static condition, the bearing speed increases linearly until it reaches the operating value of 30,000 rpm in 60 s. The acceleration is then cut off and the speed remains constant.

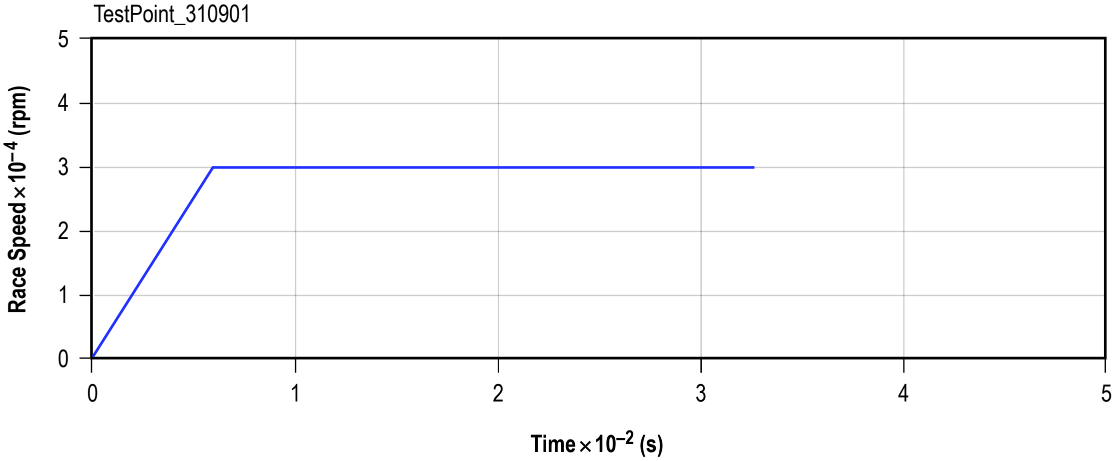

Figure 15. Race speed variation as simulated in ADORE for a typical test point.

The resulting power dissipation, or heat generation in the bearing, is shown in figure 16, along with the fraction of heat dissipated in churning and drag due to circulating LOX. Note that these solutions represent the total heat generation computed at each time step and there is no averaging of heat generation in these solutions. The distribution of time-averaged power between the circulating LOX and bearing races is shown in figure 17. Here, the computed heat generation is averaged over the selected step size, contributing to the step-wise variation.

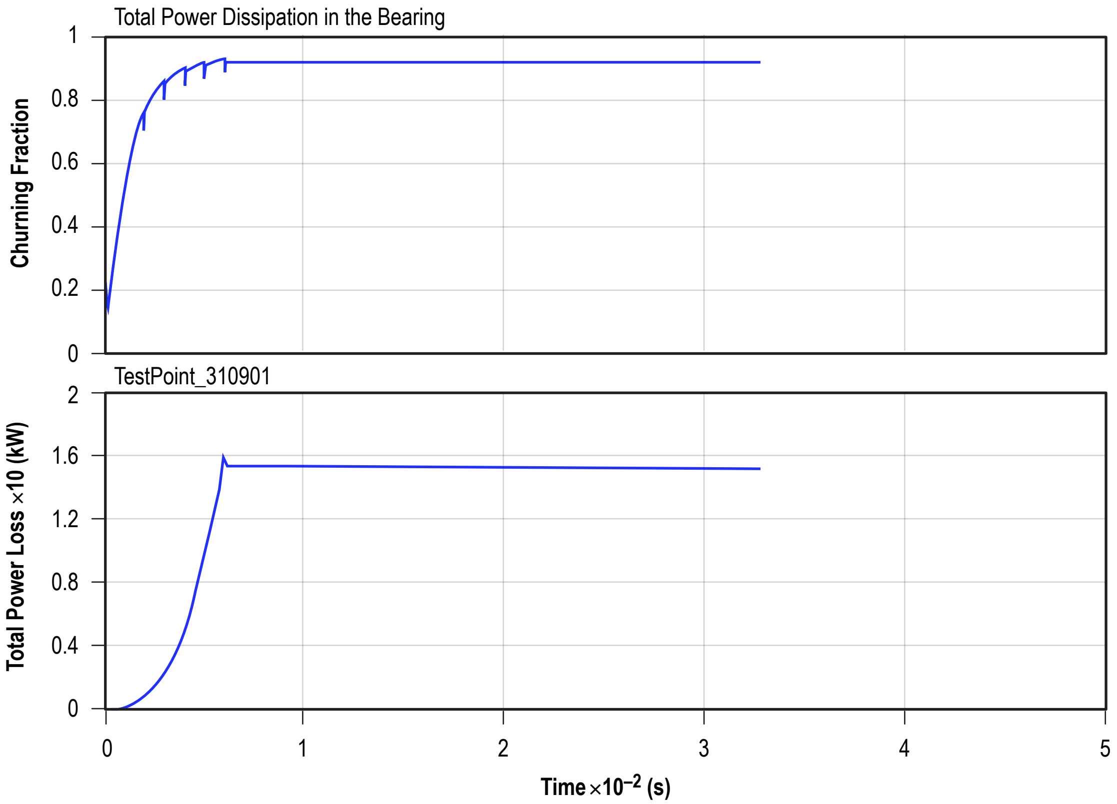

Figure 16. Simulated bearing heat generation and churning fraction for a typical test point.

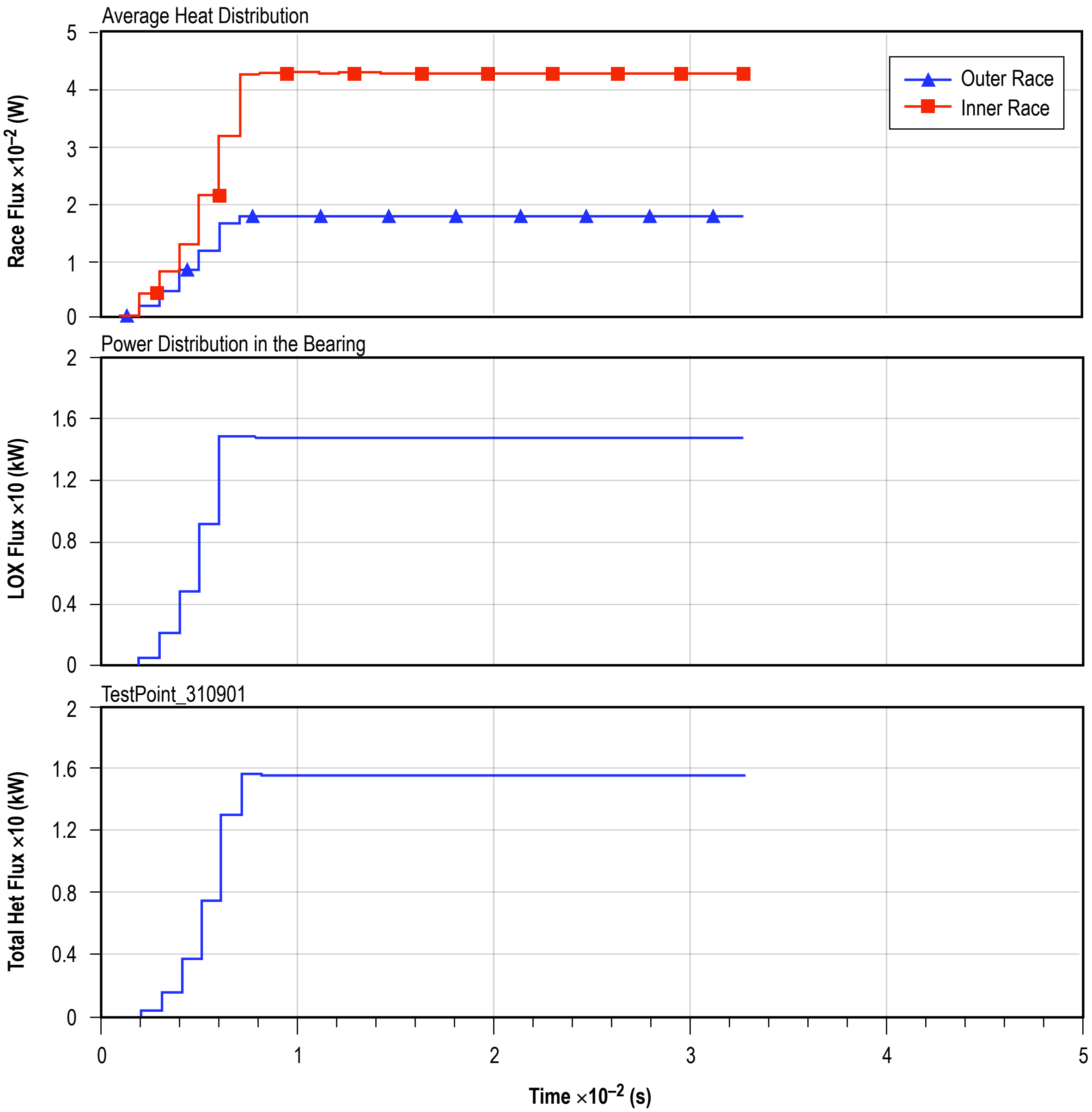

Figure 17. Average power distribution between circulating LOX and bearing races.

For an inlet LOX temperature, the computed exit temperature from the thermal interaction analysis is shown in figure 18. Again, the step-wise increase is a result of the thermal averaging algorithm. Note that the magnitude of a step change in temperature reduces as the solution converges to steady-state condition.

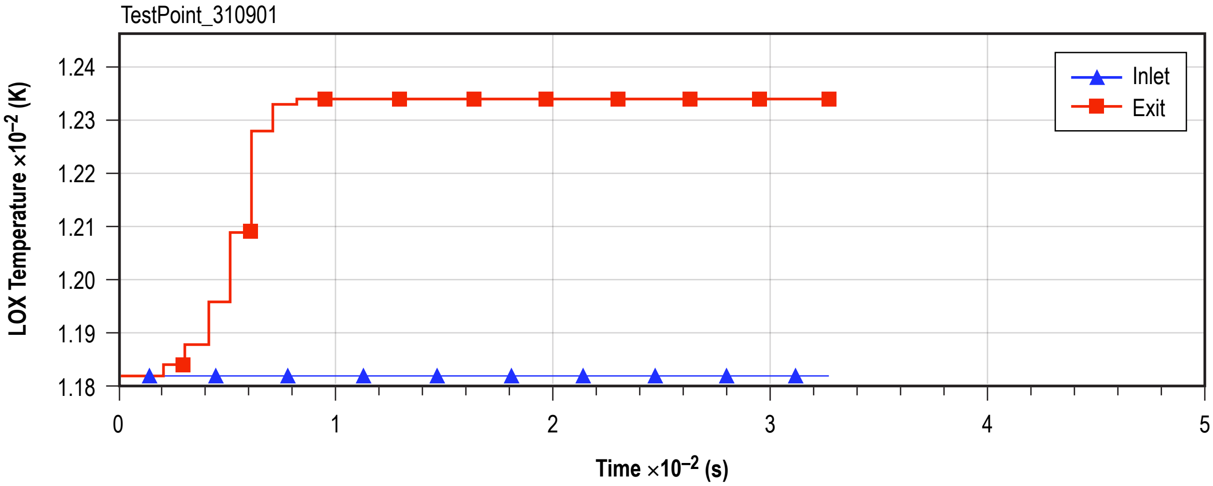

Figure 18. LOX exit temperature as simulated by ADORE for a typical test point.

For the purpose of an experimental validation, ADORE simulations for the test cases outlined in tables 2 and 3, respectively, for the 440C and hybrid bearing are obtained. As discussed earlier, experimental validation is carried out by comparing the predicted heat transferred to LOX against that estimated, per equation (16), from the experimentally measured LOX temperatures and flow rate. Validations for the 440C bearings are shown in figure 19, which plots the experimental heat transferred to LOX against that predicted by ADORE. The total heat generation, as predicted by ADORE, is also shown to demonstrate that the heat flux in circulation LOX constitutes most of the bearing heat generation. The plotted experimental value is the average of the heat flux measured for the four test bearings. Although the applied load, speed, input LOX temperature, and flow rates are identical for the four bearings in the tester, the LOX exit temperature does show a variation. Corresponding to this temperature variation, the variation in heat flux is plotted in figure 19 as a measured variation in LOX heat flux. Clearly, except for one test point, the predicted heat generation is in excellent agreement with the experimental data.

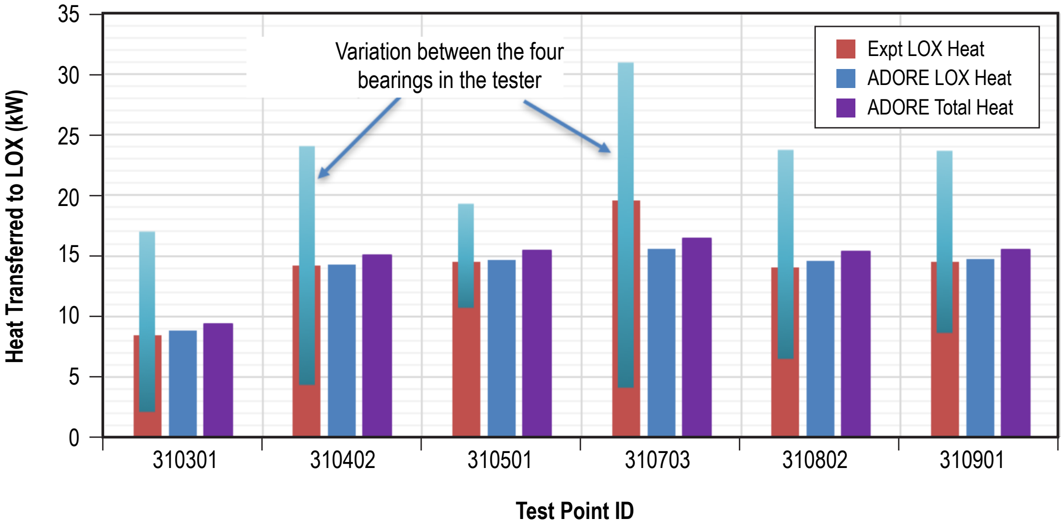

Figure 19. Variation of bearing heat generation prediction against experimental data for the 440C bearings.

A similar comparison between the experimental measurement and model predictions for the hybrid bearings is shown in figure 20. In comparison to the 400C results shown in figure 19, ADORE predictions of heat generation for hybrid bearings are somewhat lower than the experimental values. However, considering the variation in experimental data, validations are quite good.

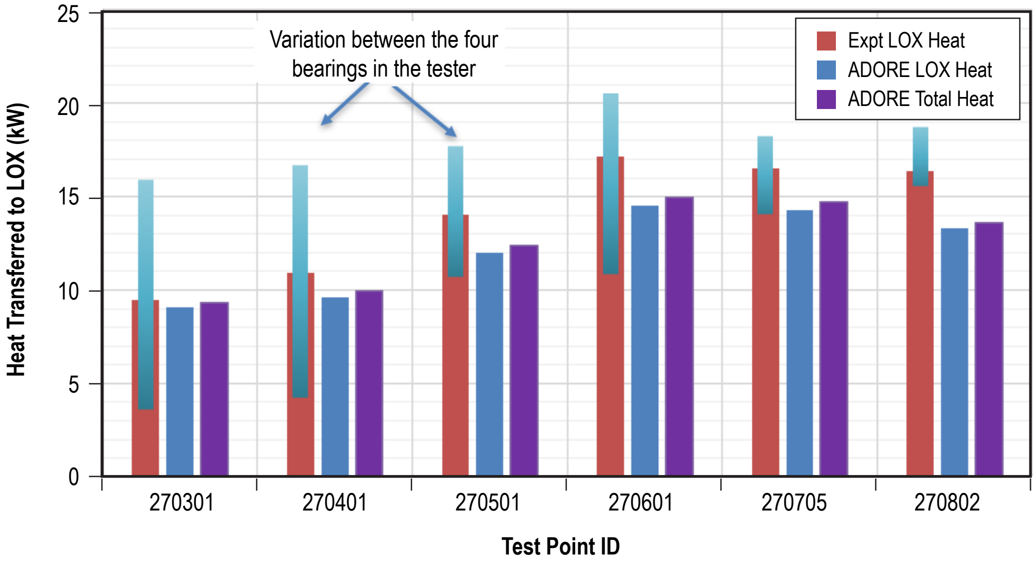

Figure 20. Validation of bearing heat generation predictions against experimental data for the hybrid bearing with 440C races and silicon nitride balls.

5. SIGNIFICANCE OF INITIAL CONDITIONS IN DYNAMIC MODELING

Dynamic bearing performance simulations obtained by integration of differential equations of motion, as done in ADORE, require initial conditions to start the integration process. A question then comes up with regard to a dependence of steady-state solution upon initial conditions. Mathematically, it may be proven that if the integration is convergent, as indicated by controlled truncation errors at each time step, then the steady-state solution does not depend on the initial conditions. Only the time required to reach steady state may depend on initial conditions. In other words, if the initial conditions are closer to the steady-state solution, then the steady-state solution may be reached earlier. In order to prove this point for the present application, an alternate solution is obtained with the operating speed as an initial condition for a typical test point.

Figure 21 shows two sets of initial conditions: (1) A variable speed case, where the race starts from zero speed and accelerates to the operating speed of 30,000 rpm and (2) a constant speed case, where the operating speed is set at 30,000 rpm upon the start of the simulation.

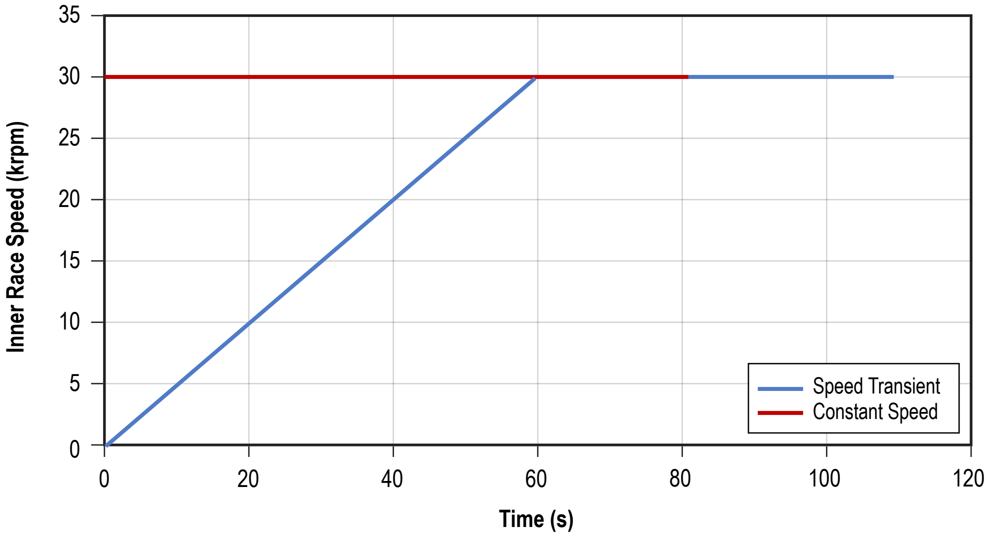

Figure 21. Constant and variable race speed as initial condition in dynamic performance simulation.

ADORE is executed for the above two sets of initial conditions for one of the test points discussed above. The computed LOX exit temperature, as determined by the thermal averaging algorithm, with the two initial conditions, is shown in figure 22. The corresponding heat transferred to LOX is plotted in figure 23. Clearly, the state solutions converge to the same values under both conditions.

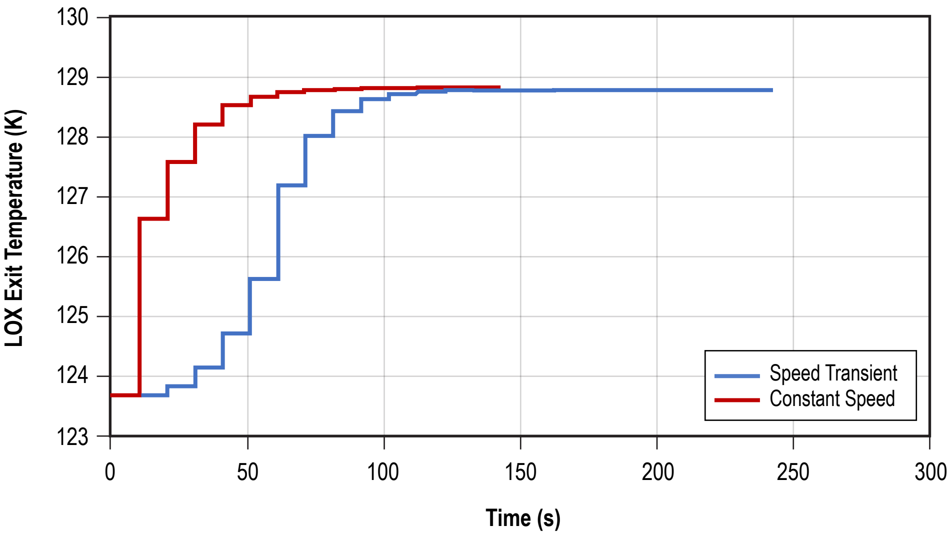

Figure 22. Comparison of LOX exit temperature solutions with the two sets of initial race speed conditions for test point 270802.

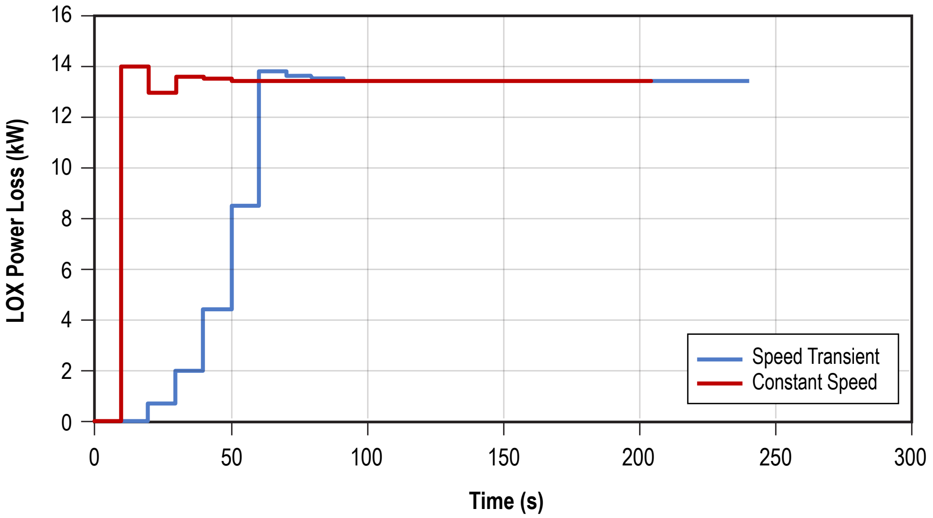

Figure 23. Heat transferred to LOX with the two sets of initial conditions for test point 270802.

The above two cases, with drastically different initial conditions, prove the independence of the steady-state solution on initial conditions. Thus, modeling of variable speed, as done in the present investigation, may not be necessary if the objective is to just determine the steady-state bearing performance.

6. PARAMETRIC EVALUATION OF HYBRID VERSUS ALL-STEEL BEARINGS

Under a prescribed contact load, operating speed, and bearing geometry, simply due to a higher modulus of elasticity of silicon nitride, the contact area is smaller and contact stress is higher in steel to silicon nitride contacts in comparison to all-steel contacts. Although the higher contact stress leads to a lower fatigue life, the smaller contact area, depending on an applicable traction coefficient, may lead to a lower contact heat generation in hybrid bearings. However, for an angular contact ball bearing with a prescribed applied load and operating speed, since the centrifugal force on silicon nitride balls is lower than that on the steel balls, both the contact load and angles in hybrid and all-steel bearings are different, even with identical bearing geometries. Therefore, a complete bearing redesign is generally essential for optimum performance with prescribed bearing materials. In the present investigation, as documented in table 1, there is a slight difference in bearing geometries for the steel and hybrid bearings. The outer race curvature factor is smaller while the internal clearance is larger for the hybrid bearings. This provides a slightly larger contact angle with the hybrid bearings. Also, as seen in figures 3 and 4, the hybrid contacts have a significantly lower traction coefficient. This greatly impacts the contact heat generation.

In order to parametrically evaluate the thermal performance of hybrid versus all-steel bearings at a typical operating speed of 30,000 rpm, a number of parametric runs are undertaken as a function of applied thrust load. Figure 24 plots the contact stresses, as determined by the applicable operating contact load and geometry. The difference between the contact stresses at the outer race between the steel and hybrid bearings is small. This is primarily a result of a more conforming race curvature in the hybrid bearing, as documented in table 1, and reduced centrifugal force on silicon nitride balls. The increased internal clearance also has an effect since it increases the contact angle. Contact stress at the inner race contact is significantly higher in the hybrid bearing since the inner race curvatures are identical in both steel and hybrid bearings. These observations suggest that, for a given application, the internal geometry of the bearing may be optimized for desired performance.

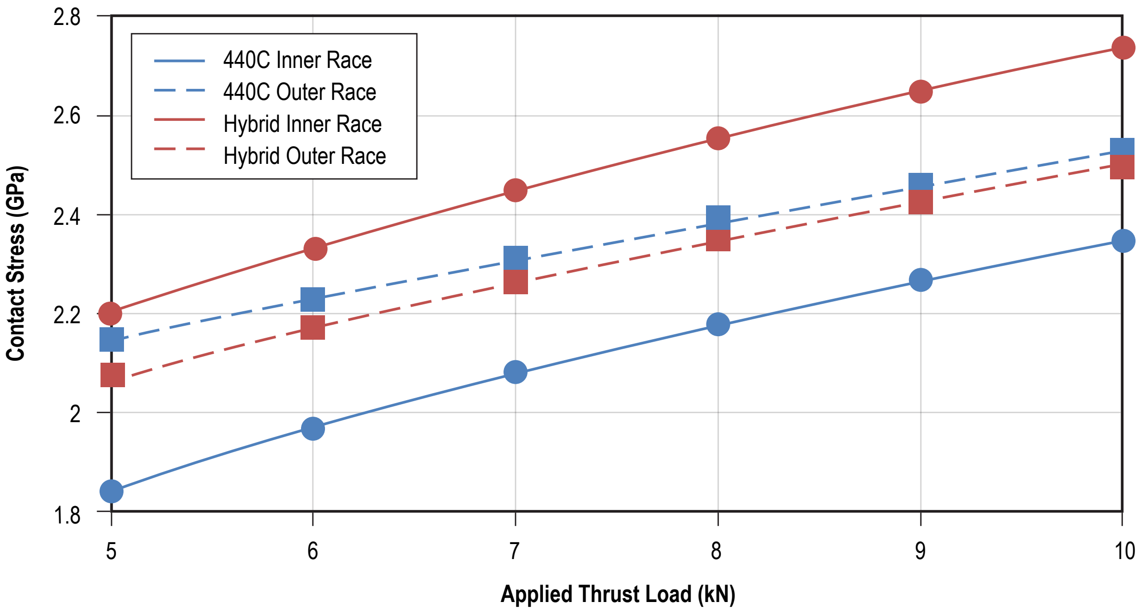

Figure 24. Comparison on ball/race contact stresses in hybrid versus all-steel bearing.

The total bearing heat generation or power loss consists of churning and drag losses and the frictional dissipation at all direct contacts between the bearing elements. Since the forces at cage contacts are quite small in comparison to the ball/race contact forces, frictional dissipation at cage contacts is generally negligible in comparison to that at the ball/race contacts. The churning and drag losses are mainly dependent on bearing speed. Therefore, at a given speed, these losses remain relatively unchanged as the applied load on the bearing increases. The frictional dissipations at ball/race contacts, on the other hand, have a strong load dependence. A comparison of the total power loss in the bearing as a function of applied load at a race speed of 30,000 rpm is presented in figure 25. Note that while the total loss is significantly lower in a hybrid bearing, the load dependence of power loss (slope of the power loss to applied load relation) is slightly stronger in an all-steel bearing compared to that in a hybrid bearing. In addition, of the smaller contact area at a given load, the lower traction coefficient in the hybrid contact, as noticed by comparing figures 3 and 4, contributes to the majority of reduction in power loss in the hybrid bearing.

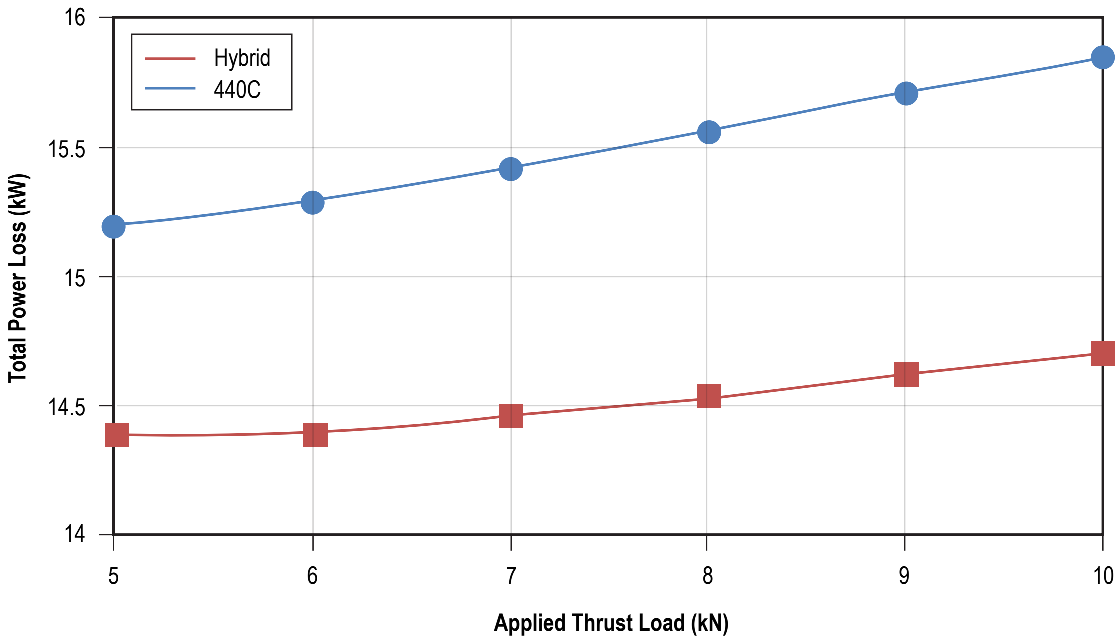

Figure 25. Comparison of total power loss between the all-steel and hybrid bearings as a function of applied thrust load at a race speed of 30,000 rpm.

While the total churning and drag is unchanged, the ratio of churning loss to total bearing loss, or the churning loss fraction, reduces as a function of applied load, as illustrated in figure 26. This is primarily due to the fact that frictional dissipation increases with increasing the load. Again, the slightly faster dropoff in churning fraction with increasing applied load is related to a faster increase of frictional dissipation in the all-steel bearing, as demonstrated in figure 25.

Since the churning and drag losses between the all-steel and hybrid bearings remain relatively unchanged, the frictional dissipation in the ball to race contacts is the principal element in evaluation of thermal performance of hybrid versus all-steel bearings. The results of figures 25 and 26 may be combined to evaluate the differences in contact losses between the all-steel and hybrid bearings. This is done in figure 27, which plots the variation in contact loss with applied thrust load. Clearly, the contact loss in a hybrid bearing is significantly lower than that in an all-steel bearing. Both the operating contact geometry and applicable traction coefficients contribute to the notable reduction in contact power loss in hybrid bearings. Furthermore, the relative reduction in contact power loss increases as the applied load increases. Such an observation demonstrates an increasing improvement in thermal performance of a hybrid bearing as the applied load increases. Again, the load dependence on these solutions is in line with those seen in figures 25 and 26.

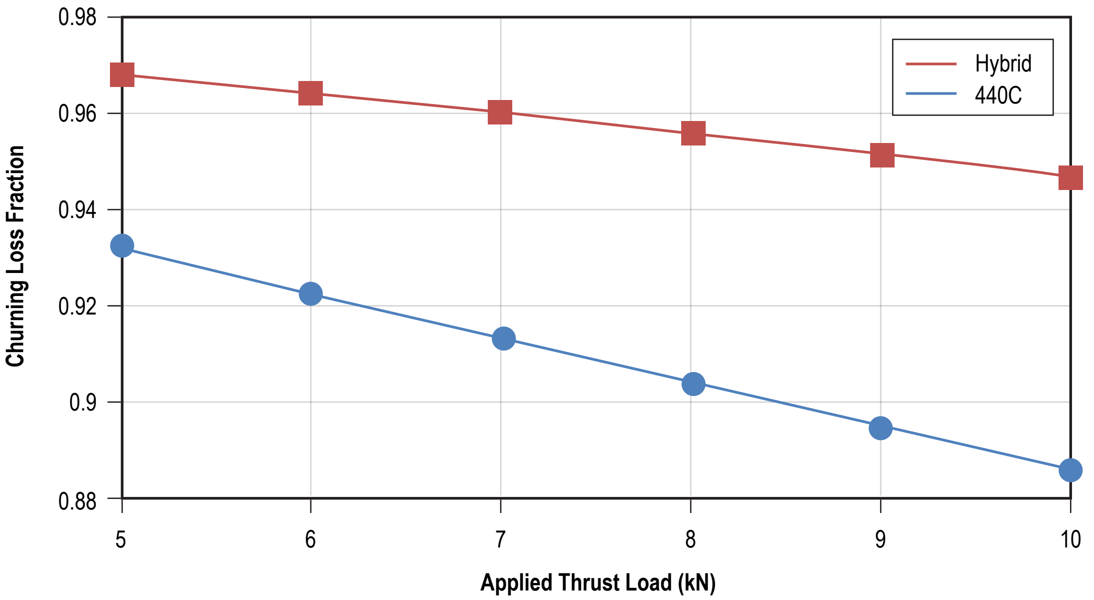

Figure 26. Variation of churning loss fraction with applied thrust load for the all-steel and hybrid bearings operating at 30,000 rpm.

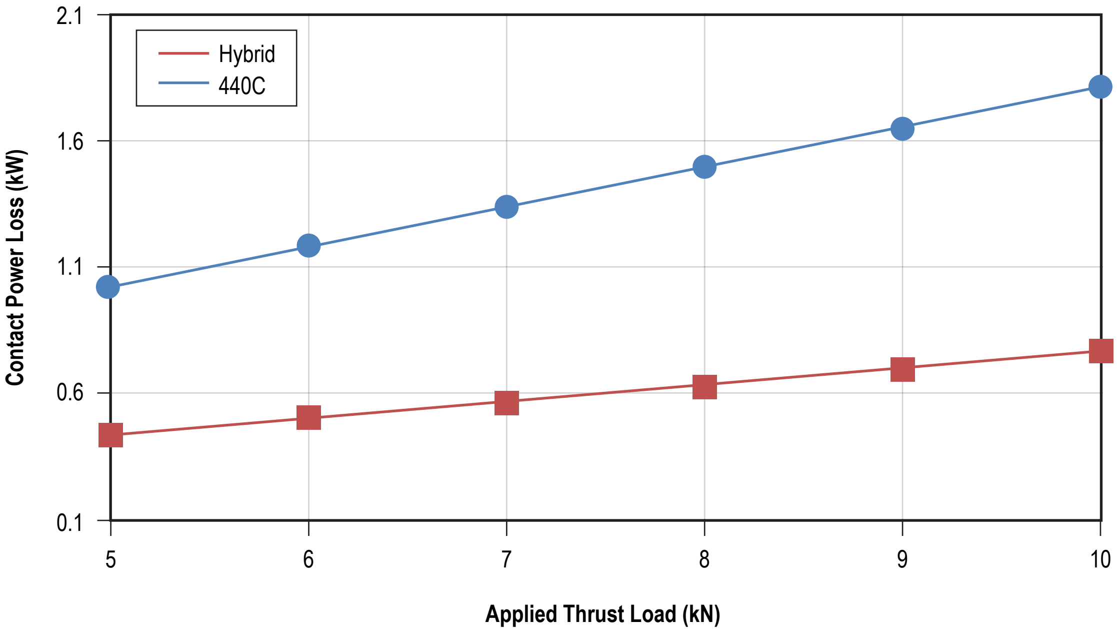

Figure 27. Comparison of contact loss as a function of applied thrust load for the all-steel and hybrid bearing at 30,000 rpm.

In a LOX environment, such a reduction in ball to race contact loss with hybrid bearings leads to improved tribological interactions at the ball/race interface and significantly improved overall bearing performance. Such a prediction is very much in line with the experimental observations reported by Moore et al.[6] Based on such parametric evaluation of thermal performance, it is anticipated that the bearing performance simulation model developed in the present investigation will serve as a viable design tool for optimizing bearing design with the prescribed materials and operating environment.

7. SUMMARY

Based on the integration of classical differential equations of motion of bearing elements, a real-time dynamic simulation of ball bearing performance is coupled with simultaneous modeling of thermal interactions between the bearing elements. The transient heat generations are time averaged over a significantly larger time step before they are used to compute the changes in bearing temperature fields. Such an averaging algorithm eliminates the numerical difficulties associated with simultaneous integration of mechanical thermal differential equations with vastly different time scales. Under stable operation, the step change in temperatures at each thermal time step converges to a steady-state solution. Following is a list of accomplishments in the present investigation:

- A real-time dynamic performance of both 440C and hybrid ball bearings in a LOX environment is modeled in both transient and steady-state time domains, as the inner race accelerates to a prescribed operating speed.

- The frictional interactions at the ball to race contacts are modeled by experimentally measured traction coefficients as a function of slide-to-roll ratios.

- Bearing heat generation, as defined by the heat transferred to circulating LOX, is validated against experimental values determined by measured LOX temperatures under prescribed pressures and flow rates. The predicted heat generation is in good agreement with the experimental values.

- The steady-state solutions are shown to be independent of initial conditions. This establishes convergence of the numerical integration of a differential equation of motion of the bearing elements.

- Churning and drag losses in the circulating LOX constitutes the majority of bearing heat generation under the experimental test conditions.

- The heat dissipated in frictional interactions in hybrid bearings is significantly lower in hybrid bearings in comparison to that simulated in all-steel bearings, while the churning and drag losses are relatively unchanged.

REFERENCES

1. Gibson, H.; Thom, R.; Moore, C.; and Haluck, D.: "History of Space Shuttle Main Engine Turbopump Bearing Testing at the Marshall Space Flight Center," NASA Technical Reports Server (NTRS), Document ID: 19980193156, <https://ntrs.nasa.gov/search.jsp?R=20100023061 2018-11-20T16:13:07+00:00Z>, 1998.

2. Crecelius, W.J.; and Pirvics, J.: "Computer Program Operating Manual on "SHABERTH", A Computer Program for the Analysis of the Steady State and Transient Thermal Performance of Shaft-Bearing Systems," U.S. Air Force Technical Report AFAP:-TR-76-90, <http://www.dtic.mil/dtic/tr/fulltext/u2/a042981.pdf>, 255 pp., July 1976.

3. SINDA, Advanced Thermal Simulation Solution, MSC Software, <http://www.mscsoftware.com/product/sinda>.

4. Gupta, P.K.: *Advanced Dynamics of Rolling Elements*, Springer-Verlag, 1984.

5. Gibson, H.G.: "An Evaluation of Bearings Operating in a Cryogenic Environment with Silicon Nitride Rolling Elements," NASA TM-103524, NASA Marshall Space Flight Center, Huntsville, AL, 20 pp., January 1991.

6. Moore, C.; Gibson, H.G.; and Thom, R.: "Liquid Hydrogen Testing of Silicon Nitride Bearings for Use in High-Speed Turbomachinery," in *Proceedings, 32nd Aerospace Mechanisms Symposium*, NASA/CP—1998–207191, Compiled by S.W. Walker and E.A. Boesiger, NASA Kennedy Space Center, FL, May 13–15, 1998, pp. 197–211, 1998.

7. Tevaarwerk, J.L.: "Development of a Cryogenic Traction Tester," NASA Contract No. NAS8-38552, NASA Marshall Space Flight Center, Huntsville, AL, 1992.

8. Chang, L.; Hall, P.B.; and Thom, R.: "Scuffing Characteristics of High-Load Rolling/Sliding Contacts Operating in Liquid Oxygen—Effects of Materials and Surface Roughness," *Tribology Transactions*, Vol. 41, No. 1, pp. 87–95, doi.org/10.1080/10402009808983725, March 25, 1998.

9. Moore, J.D.: *SSME Bearing and Seal Tester Data Compilation, Analysis, and Reporting*: *And Refinement of the Cryogenic Bearing Analysis Mathematical Model*, SRS Technologies Technical Report prepared under NASA Contract NAS8-39379, 2000.

10. Gibson, H.G.; Thom, R.; and Moore, C.: "Space Shuttle Main Engine Turbopump Bearing Testing at Marshall Space Flight Center," Conference Paper, Report #M10-0202, NASA Technical Reports Server (NTRS), Document ID: 20100022057, 57th JANNAF Joint Propulsion Meeting, May 3–7, 2010, Colorado Springs, CO, 2010.

11. Lemmon, E.W.; Bell, I.H.; Huber, M.L.; and McLinden, M.O.: “NIST Standard Reference Database 23: Reference Fluid Thermodynamic and Transport Properties-REFPROP, Version 10.0, National Institute of Standards and Technology, Standard Reference Data Program, Gaithersburg, MD, 2018.

12. Schlichtig, H.: *Boundary Layer Theory*, McGraw Hill, pp. 15–19, 93–99, 606–608, 1968.

13. Gupta, P.K.: “Thermal Interactions in Rolling Bearing Dynamics,” Air Force Technical Report AFRL-PR-WP-TR-2002-2042, <http://www.dtic.mil/dtic/tr/fulltext/u2/a409914.pdf>, March 2002.

14. McAdams, W.H.: *Heat Transmission*, McGraw-Hill, New York, pp. 265–268, 1954.

15. Kreith, F.: *Principals of Heat Transfer*, 2nd ed., International Text Book Co, pp. 410–415, 1966.

16. Rohsenow, W.H.; and Choi, H.Y.: *Heat Mass and Momentum Transfer*, Prentice Hall, pp. 200–202, June 1, 1961.

REPORT DOCUMENTATION PAGE

Form Approved
OMB No. 0704-0188

1. REPORT DATE *(DD-MM-YYYY)*
01–03–2019

2. REPORT TYPE
Technical Publication

3. DATES COVERED *(From - To)*

4. TITLE AND SUBTITLE
Real-Time Modeling of Thermal Interactions
in Cryogenic Ball Bearings

5a. CONTRACT NUMBER

5b. GRANT NUMBER

5c. PROGRAM ELEMENT NUMBER

6. AUTHOR(S)
P.K. Gupta* and H.G. Gibson

5d. PROJECT NUMBER

5e. TASK NUMBER

5f. WORK UNIT NUMBER

7. PERFORMING ORGANIZATION NAME(S) AND ADDRESS(ES)
George C. Marshall Space Flight Center
Huntsville, AL 35812

8. PERFORMING ORGANIZATION REPORT NUMBER
M–1481

9. SPONSORING/MONITORING AGENCY NAME(S) AND ADDRESS(ES)
National Aeronautics and Space Administration
Washington, DC 20546–0001

10. SPONSORING/MONITOR'S ACRONYM(S)
NASA

11. SPONSORING/MONITORING REPORT NUMBER
NASA/TP—2019–220130

12. DISTRIBUTION/AVAILABILITY STATEMENT
Unclassified-Unlimited
Subject Category 20
Availability: NASA STI Information Desk (757–864–9658)

13. SUPPLEMENTARY NOTES
Prepared by the Materials and Processes Laboratory, Engineering Directorate
*PKG Inc., Clifton Park, NY

14. ABSTRACT

Real-time modeling of thermal interactions in cryogenic ball bearings is based on integration of classical differential equations of motion of bearing elements. Time-averaging of transient heat generations in the bearing is implemented to model temperature fields in the bearing under vastly different thermal and mechanical time scales. Both all-steel and hybrid bearings for liquid oxygen (LOX) turbopump applications are modeled. Bearing performance simulations are closely modeled over experimental time cycles under both transient and steady-state domains. Steady-state solutions are shown to be independent of initial conditions to demonstrate acceptable convergence of time domain integrations. Model predictions of the majority of bearing heat generation, as computed by the predicted LOX exit temperature under prescribed inlet temperature, pressure, and flow rate, are validated against those measured experimentally. The model predictions are in good agreement with experimental measurements for both all-steel and hybrid bearings. Churning and drag losses contribute to the majority of the total heat generation in the test bearings. Under prescribed applied load and speed, while the ball/race contact stress is higher in hybrid bearings, the contact heat generation is significantly lower in comparison to that in an all-steel bearing, particularly under heavily loaded high-speed conditions.

15. SUBJECT TERMS
bearing modeling, ADORE, turbopump bearings, bearing, computer modeling, turbopump

16. SECURITY CLASSIFICATION OF: a. REPORT	b. ABSTRACT	c. THIS PAGE	17. LIMITATION OF ABSTRACT	18. NUMBER OF PAGES	19a. NAME OF RESPONSIBLE PERSON
U	U	U	UU	52	STI Help Desk at email: help@sti.nasa.gov
					19b. TELEPHONE NUMBER *(Include area code)* STI Help Desk at: 757–864–9658

National Aeronautics and
Space Administration
IS02
George C. Marshall Space Flight Center
Huntsville, Alabama 35812